Mathematical Biology



Phase field modeling and computation of vesicle growth or shrinkage

Xiaoxia Tang¹ · Shuwang Li¹ · John S. Lowengrub² · Steven M. Wise³ ₪

Received: 3 October 2022 / Revised: 1 February 2023 / Accepted: 7 April 2023 /

Published online: 23 May 2023

© The Author(s), under exclusive licence to Springer-Verlag GmbH Germany, part of Springer Nature 2023

Abstract

We present a phase field model for vesicle growth or shrinkage induced by an osmotic pressure due to a chemical potential gradient. The model consists of an Allen-Cahn equation describing the evolution of the phase field parameter that describes the shape of the vesicle and a Cahn-Hilliard-type equation describing the evolution of the ionic fluid. We establish conditions for vesicle growth or shrinkage via a common tangent construction using free energy curves. During the membrane deformation, the model ensures total mass conservation of the ionic fluid, and we weakly enforce a surface area constraint of the vesicle. We develop a stable numerical scheme and an efficient nonlinear multigrid solver to evolve the phase and concentration fields, and we use this to evolve the fields to near equilibrium for 2D vesicles. Convergence tests confirm an $\mathcal{O}(t+h^2)$ accuracy for our scheme and near-optimal convergence for our multigrid solver. Numerical results reveal that the diffuse interface model captures the main features of cell shape dynamics: for a growing vesicle, there exist circle-like equilibrium shapes if the concentration difference across the membrane and the initial osmotic pressure are large enough; while for a shrinking vesicle, there exists a rich collection of finger-like equilibrium morphologies.

Steven M. Wise swisel @utk.edu

Xiaoxia Tang xtang15@hawk.iit.edu

Shuwang Li sli@ math.iit.edu

John S. Lowengrub jlowengr@uci.edu

- Department of Applied Mathematics, Illinois Institute of Technology, Chicago, IL 60616, USA
- Department of Mathematics, The University of California, Irvine, CA 92697, USA
- Department of Mathematics, The University of Tennessee, Knox ville, TN 37996, USA



97 Page 2 of 31 X. Tang et al.

Keywords Allen–Cahn equation \cdot Cahn–Hilliard equation \cdot Osmosis \cdot Vesicle growth or shrinkage \cdot Nonlinear multigrid \cdot Convergence

Mathematics Subject Classification $65M06 \cdot 65M12 \cdot 65M55 \cdot 76T99$

1 Introduction

Membranes considered in this paper are composed of bilayer lipid molecules with hydrophilic heads and two hydrophobic hydrocarbon chains. Lipid bilayers are the basic structural component of biological membranes. It is a semipermeable barrier to most solutes, including ions, proteins and other molecules. In an aqueous environment, a bilayer lipid membrane forms a vesicle (a closed bio-membrane containing fluid) to reduce the energy of the hydrophobic edges. Because of their relatively simple structure, vesicles are often used as a model system for studying fundamental physics underlying complicated biological systems such as cells and microcapsules. In addition, vesicles have also been used as building blocks to engineer artificial cells, e.g., via biochemical microreactors operating in physiological environments (Elani et al. 2014).

Osmosis usually refers to the net movement of water molecules across a semipermeable membrane driven by a difference in concentration of solute on either side (Alberts et al. 2022; Baumgarten and Feher 2012; Strange 2004). Tonicity is a related concept, operationally defined as the ability of a solution to shrink or swell specified cells. Hypotonicity describes any medium with a sufficiently low concentration of solutes to drive water to move into a cell due to osmosis. Hypertonicity describes any medium with a sufficiently high concentration of solutes to drive water to move out of a cell due to osmosis (Alberts et al. 2022; Baumgarten and Feher 2012). In Fig. 1, we show response of a human red blood cell to changes in tonicity with respect to the extracellular fluid. Clearly, hypertonic solutions shrink cells; hypotonic solutions increase cell volume; and isotonic solutions neither swell nor shrink the cell. Biologically, cells change their volumes, due to different environmental conditions, through the influx or efflux of water (the primary solvent) based on differing concentrations of an ionic solute or pressure gradients (Hoffmann et al. 2009; Guo 2017). The mechanical properties of cells can change, as the volume changes. For example, the cell may become more stiff as the volume is decreased, due to crowding of cellular structures (Hoffmann et al. 2009). Motivated by these volume changes, in this paper, we develop a mathematical model to simulate the effects of growth or shrinkage coming from the concentration gradient. For simplicity, in this first modeling effort, we will neglect differences in cell rigidity due to changing volume.

Mathematical modeling of membrane deformation has become an important area of research in biological materials for the past 15 years. At the continuum level, the mathematical description of vesicle conformation and deformation is a highly nonlinear, nonlocal moving boundary problem, where the bilayer membrane serves as the moving boundary. Sharp interface models have been implemented to simulate the motion of vesicles in fluids in (Veerapaneni et al. 2009a, b; Sohn et al. 2010; Salac and Miksis 2011; Sohn et al. 2012; Li et al. 2012; Haußer et al. 2013; Liu et al. 2016; Gera



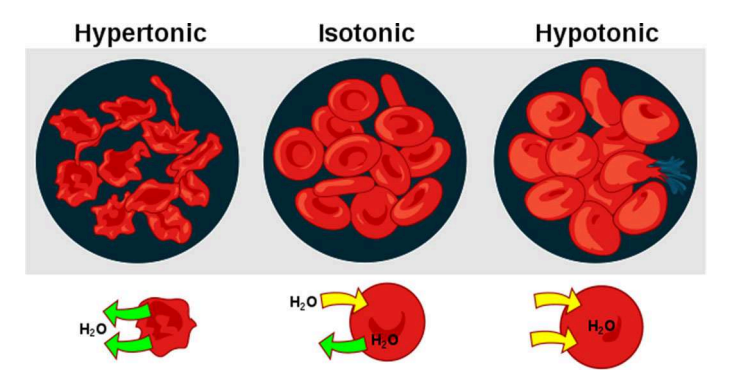


Fig. 1 Effect of different solutions on human red blood cells. The cell swells, shrinks or stays normal as water moves into or out of the cell down its concentration gradient in hypotonic, hypertonic, or isotonic solutions, respectively. From Wikipedia, the Free Encyclopedia. https://en.wikipedia.org/wiki/Tonicity (LadyofHats 2007)

and Salac 2018; Gera et al. 2022). For example, nonlinear wrinkling dynamics of a vesicle in an extensional flow and tumbling mechanism of two-dimensional vesicles in a shear flow are studied in Liu and Li (2014); Liu et al. (2017). These sharp interface models can satisfy the interface and inextensibility conditions exactly. That is, the volume enclosed by membrane is automatically conserved for an incompressible fluid. The deformation based on the net mass transfer (gain or loss) across the membrane has not been considered, to our knowledge. There are also sharp interface models of membrane deformation based on osmosis and diffusion (Layton 2006; Vogl et al. 2014; Jayathilake et al. 2010a, b; Mori et al. 2001; Yao and Mori 2017; Wang et al. 2020; Quaife et al. 2021). For example, boundary integral simulations are used to investigate the effects of water permeability on the hydrodynamics of an inextensible membrane under a mechanical load in Quaife et al. (2021). An immersed boundary method (Peskin 1977) for modeling convection and diffusion of mass transfer through porous membranes under large deformations is proposed in a recent paper (Wang et al. 2020).

Phase field/diffuse interface models have also been used to simulate the equilibrium configurations and the dynamics of vesicles (Du et al. 2004; Wang and Du 2008; Lowengrub et al. 2009; Gu et al. 2016). Typically phase field models are constructed so as to approximate a sharp interface counterpart, solutions of the former converging to those of the later as the diffuse interface thickness, usually denoted ε , goes to zero. The interface separating the inside from the outside of a vesicle is modeled as a continuous, diffuse boundary layer, in a phase field variable (Giga et al. 2017; Kobayashi 2010). One advantage of the phase field approach is its simplicity in model formulation; the interface problem is posed as a reaction-diffusion equation defined on the whole computational domain without requiring special treatment at the interface. This makes numerical implementation a simple matter, generally. In this approach, updating the interface position is a simple matter of advancing the phase field in time (Shen et al. 2012; Kobayashi 2010; Provatas and Elder 2010). The well known Allen–Cahn (AC) and Cahn–Hilliard (CH) equations are two diffuse interface gradient flow type PDEs



97 Page 4 of 31 X. Tang et al.

describing the process of phase separation of a binary mixture. The field variable is conserved in the CH equation, but non-conserved in AC equation (Giga et al. 2017; Bartels 2015; Lee et al. 2014). More generally, the models are designed so that a free energy is dissipated in time, while the phase field is either conserved or not, based on the physics of the problem at hand.

In this paper, we develop a phase field model to simulate vesicle growth or shrinkage based on osmotic pressure, which arises due to a chemical potential gradient. In particular, we determine control conditions for growth and shrinkage via a common tangent construction. We simulate the growth and shrinkage effects subject to total mass conservation and surface area constraint, while allowing the mass exchange inside and outside the vesicle. Considering surface bending energy, osmotic pressure energy, and a surface area constraint in addition to the surface energy used in the classical AC and CH equations, we derive a coupled system of equations consisting of an AC equation describing the evolution of the vesicle phase field and a conserved CH equation describing the evolution of concentration field.

To avoid severe CFL-like time step restrictions, we employ a first-order (in time) implict-explicit numerical scheme to advance the fields in time. We discretize space using a standard second-order finite difference method. The scheme is solved by a Full Approximation Storage (FAS) nonlinear multigrid scheme, like that proposed in Wise (2010). More information on nonlinear multigrid methods can be found in Trottenberg et al. (2001), Henson (2003), Kay and Welford (2006). The solver we constructed uses a Gauss–Seidel-based smoother and a V-Cycle method for transferring information among multigrid levels. In numerical tests, we demonstrate the nearly optimal complexity of the multigrid solver, and we demonstrate convergence of the time-stepping scheme, which is of first order in time and second order in space. Numerical results reveal that for a growing vesicle, there exist circle-like equilibrium shapes if the concentration difference across the membrane and the initial osmotic pressure are large enough; while for a shrinking vesicle, there exists a rich collection of finger-like equilibrium morphologies.

This paper is organized as follows. In Sect. 2, we define the model equations and analyse conditions for vesicle growth or shrinkage by a common tangent construction. In Sect. 3, the numerical scheme of the system and nonlinear multigrid algorithm are presented. Numerical results are given in Sect. 4.

2 Model formulation

2.1 Evolution equations

We start by defining a Helmholtz free energy, F, over a computational domain, $\Omega \subset \mathbb{R}^d$, d=2 or 3. The functions ϕ , $\psi:\Omega\to\mathbb{R}$ are the phase fields (order parameters) describing the vesicle shape and the concentration of ionic fluid occupying the volume Ω , respectively. $\{\mathbf{x}:\phi(\mathbf{x})=0\}$ determines the location of the membrane, while $\{\mathbf{x}:\phi(\mathbf{x})=1\}$ represents the interior phase (inside the vesicle), and $\{\mathbf{x}:\phi(\mathbf{x})=-1\}$ represents the exterior phase (outside the vesicle). We consider the following free energy densities (Cahn and Hilliard 1958; Du et al. 2004, 2005; Wang and Du 2008:



$$f^{\text{surf}}(\phi, \nabla \phi) := \frac{3\sqrt{2}}{4} \left(\frac{1}{\varepsilon} g(\phi) + \frac{\varepsilon}{2} |\nabla \phi|^2 \right),$$
 (2.1)

$$f^{\text{bend}}(\phi, \Delta \phi) := \frac{3\sqrt{2}}{16\varepsilon} \left(\frac{1}{\varepsilon} g'(\phi) - \varepsilon \Delta \phi\right)^2,$$
 (2.2)

$$f^{\text{osm}}(\phi, \psi) := \frac{1 + p(\phi)}{2} f^{\text{in}}(\psi) + \frac{1 - p(\phi)}{2} f^{\text{out}}(\psi), \tag{2.3}$$

where g is the standard double-well function $g(\phi) = \frac{1}{4} (\phi^2 - 1)^2$; ε is a small positive constant characterizing the thickness of the diffuse interface; and $f^{\rm in}(\psi)$ and $f^{\rm out}(\psi)$ are quadratic functions

$$f^{\text{in}}(\psi) := \frac{\gamma_{\text{in}}}{2} (\psi - \psi_{\text{in}})^2 + \beta_{\text{in}} \quad \text{and} \quad f^{\text{out}}(\psi) := \frac{\gamma_{\text{out}}}{2} (\psi - \psi_{\text{out}})^2 + \beta_{\text{out}},$$
(2.4)

where γ_{in} , ψ_{in} , β_{in} , γ_{out} , ψ_{out} , β_{out} are assumed to be positive parameters. The function p is an interpolation function satisfying p(1) = 1 (interior phase) and p(-1) = 1-1 (exterior phase) and p'(-1) = p'(1) = 0, as well. Now, we define free energies

$$F^{\text{surf}} := \int_{\Omega} \gamma_{\text{surf}} f^{\text{surf}}(\phi, \nabla \phi) \, dx, \qquad (2.5)$$

$$F^{\text{bend}} := \int_{\Omega} \gamma_{\text{bend}} f^{\text{bend}}(\phi, \Delta \phi) \, d\mathbf{x}, \qquad (2.6)$$

$$F^{\text{area}} := \frac{\gamma_{\text{area}}}{2} \left(\int_{\Omega} f^{\text{surf}}(\phi, \nabla \phi) \, d\mathbf{x} - A \right)^2, \tag{2.7}$$

$$F^{\text{osm}} := \int_{\Omega} f^{\text{osm}}(\phi, \psi) \, dx. \tag{2.8}$$

 F^{surf} is the diffuse interface approximation of the total surface area of the vesicle. F^{bend} is the diffuse interface approximation of the surface bending energy. A is the initial surface area of the vesicle. F^{area} is the energy penalty to numerically enforce the surface area constraint, since the surface area should remain approximately unchanged for a vesicle with a fixed number of lipids. The constants γ_{surf} , γ_{bend} , γ_{area} are assumed positive. The ε dependencies in the free energy terms F^{surf} and F^{bend} are chosen so as to give the correct asymptotic limits as $\varepsilon \to 0$. Specifically, in the limit $\varepsilon \to 0$, these terms approximate singular sharp interface counterparts (see Du et al. 2005, 2004; Wang and Du 2008) for details. F^{osm} describes the osmotic energy arises in the mixture fluids with different concentrations. The total Helmholtz free energy is thus defined as

$$F[\phi, \psi] = F^{\text{surf}}[\phi] + F^{\text{bend}}[\phi] + F^{\text{area}}[\phi] + F^{\text{osm}}[\phi, \psi]. \tag{2.9}$$



97 Page 6 of 31 X. Tang et al.

The dynamical equations are of gradient flow type with respect to the free energy, F:

$$\partial_t \phi = -M_\phi \mu, \tag{2.10}$$

$$\mu = \delta_{\phi} F, \tag{2.11}$$

$$\partial_t \psi = \nabla \cdot \left(M_{\psi}(\phi) \nabla \nu \right), \tag{2.12}$$

$$\nu = \delta_{yt} F, \tag{2.13}$$

where the phase variable ϕ is non-conserved and satisfies an Allen–Cahn equation, while the variable ψ , since it represents the ionic fluid, is conserved and satisfies a Cahn–Hilliard-type mass conservation equation. We take homogeneous Neumann boundary conditions on the computational boundary $\partial \Omega$. Here the mobility $M_{\phi} > 0$ is a constant and $M_{\psi}(\phi) > 0$ is a positive function of ϕ . μ and ν are the chemical potentials

$$\mu = \delta_{\phi} F = \gamma_{\text{surf}} \frac{3\sqrt{2}}{4} \omega + \gamma_{\text{bend}} \frac{3\sqrt{2}}{8} \left(\frac{\omega}{\varepsilon^{2}} g''(\phi) - \Delta \omega \right)$$

$$+ \gamma_{\text{area}} \left(\int_{\Omega} f^{\text{surf}}(\phi, \nabla \phi) d\mathbf{x} - A \right) \frac{3\sqrt{2}}{4} \omega$$

$$+ \frac{p'(\phi)}{2} \left(f^{\text{in}}(\psi) - f^{\text{out}}(\psi) \right), \qquad (2.14)$$

$$\omega = \frac{1}{\varepsilon} g'(\phi) - \varepsilon \Delta \phi, \tag{2.15}$$

$$v = \delta_{\psi} F = \frac{1 + p(\phi)}{2} \cdot \frac{df^{\text{in}}}{d\psi}(\psi) + \frac{1 - p(\phi)}{2} \cdot \frac{df^{\text{out}}}{d\psi}(\psi). \tag{2.16}$$

It is reasonable to assume that the mobility for ψ degenerates in the interfacial region, since mass flow is limited to small channels in the vesicle membrane. Therefore, we assume that

$$M_{\psi}(\phi) = 1 - M_0(\phi^2 - 1)^2$$
, for some $M_0 \in (0, 1)$, (2.17)

and it follows that $M_{\psi} \ge 1 - M_0 > 0$. The system (2.10)–(2.13) is free energy dissipative, and the dissipation rate is

$$d_{t}F = \int_{\Omega} \left\{ \delta F_{\phi} \partial_{t} \phi + \delta F_{\psi} \partial_{t} \psi \right\} d\mathbf{x}$$

$$= \int_{\Omega} \left\{ \mu \partial_{t} \phi + \nu \partial_{t} \psi \right\} d\mathbf{x}$$

$$= \int_{\Omega} \left\{ \mu \left(-M_{\phi} \mu \right) + \nu \left(\nabla \cdot \left(M_{\psi} \nabla \nu \right) \right) \right\} d\mathbf{x}$$

$$= \int_{\Omega} \left\{ -M_{\phi} |\mu|^{2} - M_{\psi} |\nabla \nu|^{2} \right\} d\mathbf{x}$$

$$\leq 0$$



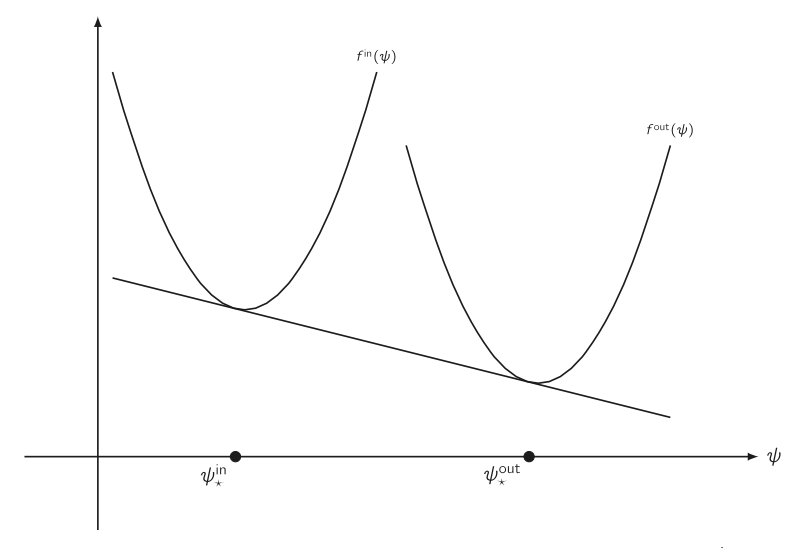


Fig. 2 Typical common tangent connection for the free energy densities for the interior $f^{\text{in}}(\psi)$ (left) and exterior $f^{\text{out}}(\psi)$ (right) (2.4) phases. The vesicle will grow or shrink according to the initial (spatially uniform) states for ψ inside and outside the vesicle. Suppose that $\psi_{\mathbf{i}}^{\mathbf{in}}$ and $\psi_{\mathbf{v}}^{\text{out}}$ are the values of ψ where the common tangent touches the respective free energy densities $f^{\text{in}}(\psi)$ (left) and $f^{\text{out}}(\psi)$ (right)

Next, we analyse the conditions for vesicle growth or shrinkage via the common tangent construction based on the osmotic free energy.

2.2 Conditions for growth or shrinkage

Suppose that ψ_{\star}^{in} and $\psi_{\star}^{\text{out}}$ are the equilibrium concentration values for the interior and exterior regions obtained via the common tangent construction (Provatas and Elder 2010; Pelton 2019), and let us further assume that

$$\psi_{\star}^{\text{in}} < \psi_{\star}^{\text{out}}, \tag{2.18}$$

as shown in Fig. 2. Now, suppose that we choose the following initial conditions for ψ :

$$\psi^{\text{in}}(t=0) =: \psi_0^{\text{in}} < \psi_{\star}^{\text{in}} \text{ and } \psi^{\text{out}}(t=0) =: \psi_0^{\text{out}} = \psi_{\star}^{\text{out}}.$$
 (2.19)

This is the case that is illustrated in Fig. 3. The exterior phase is at its bulk equilibrium value, but the interior phase is not. The osmotic free energy is decreased as the concentration in the interior region goes up from the initial value ψ_0^{in} to the equilibrium value ψ_{\star}^{in} . Therefore mass will flow from outside the vesicle to the inside until a global equilibrium is attained. In this case, the mass will be transferred into the interior region (the volume of the vesicle will increase), though its surface area will ideally remain unchanged.



97 Page 8 of 31 X. Tang et al.

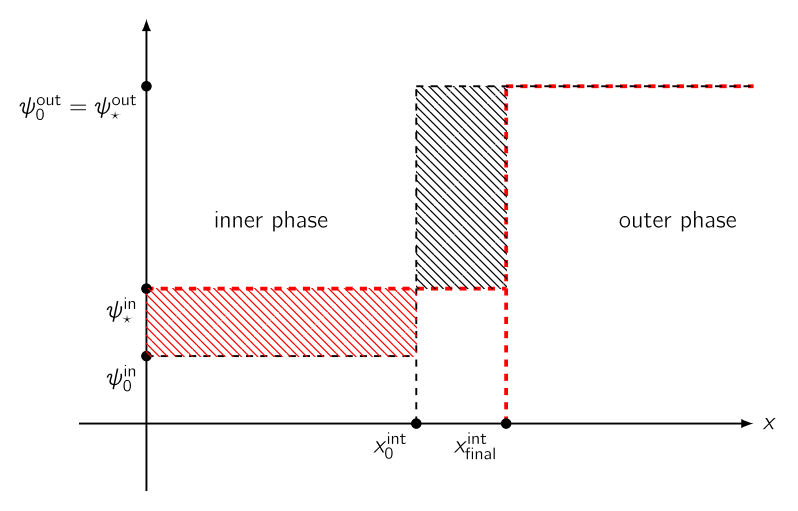


Fig. 3 An example of volumetric growth. The black dashed regions show the initial state, and the red shows the final state. x_0^{int} is the initial position of the interface; $x_{\text{final}}^{\text{int}}$ is the position of the interface after global equilibrium is attained. The total mass is conserved; mass from the black region is transferred into the red region. The interface moves to the right, and the concentration in the inner phase increases (color figure online)

The shrinkage case is analogous and is illustrated in Fig. 4. Suppose the initial conditions for this case are

$$\psi^{\text{in}}(t=0) =: \psi_0^{\text{in}} > \psi_{\star}^{\text{in}} \text{ and } \psi^{\text{out}}(t=0) =: \psi_0^{\text{out}} = \psi_{\star}^{\text{out}}.$$
 (2.20)

In this case, the mass will be transferred into the exterior region, and the interior region will shrink (the volume of the vesicle decreases with constant surface area) as the osmotic free energy decreasing, while the concentration in the interior region decreases from its initial value ψ_0^{in} to the equilibrium value ψ_*^{in} .

3 Numerical method

In this section, we describe a semi-implicit Euler scheme for time discretization and a centered difference finite difference method for spatial discretization to get a semi-implicit numerical scheme, then solve the discrete system by a nonlinear FAS multigrid method, which is the combination of a nonlinear Gauss–Seidel smoothing (relaxation) operator and V-cycle multigrid solver. There have been many numerical works for the Allen–Cahn and Cahn–Hilliard equations based on convex splitting (Wise 2010; Hu et al. 2009) and other approaches. Two important properties that convex splitting schemes generally inherit are unconditional energy stability and unconditional unique solvability. The convex splitting methods require the splitting of the free energy into purely convex and concave pieces. But, for our model, the convex splitting approach is difficult to apply due to the fact that such a splitting is highly nontrivial. Alternatively, we could employ an scalar auxiliary variable (SAV) approach, which makes the process of finding stable and even linear schemes much easier (Shen et al. 2018). However, in



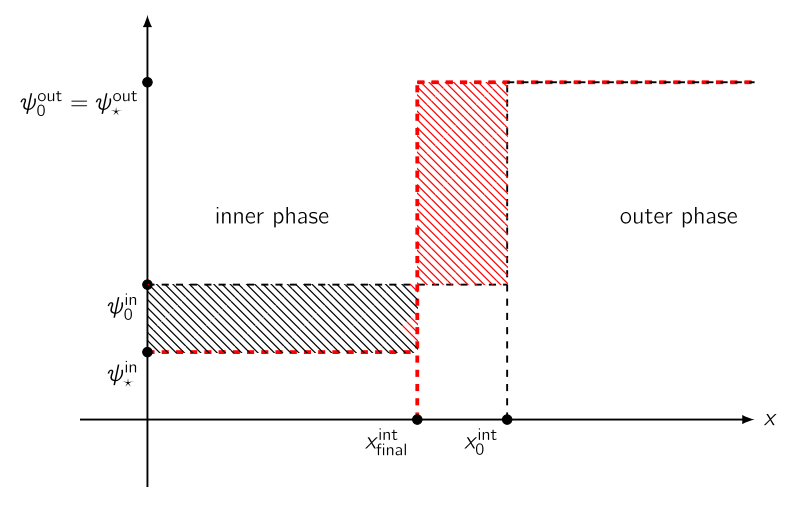


Fig. 4 An example of volumetric shrinkage. The black dashed regions show the initial state, and the red shows the final state. x_0^{int} is the initial position of the interface; $x_{\text{final}}^{\text{int}}$ is the position of the interface after global equilibrium is attained. The mass is conserved; mass from the black region is transferred into the red region. The interface moves to the left and the concentration in the inner phase decreases (color figure online)

this paper, the design of theoretically stable numerical methods is not the focus, and we will save these issues for a follow-up paper.

3.1 Discretization of time

The evolution equation are expected to be numerically stiff, since they are nonlinear parabolic equations of fourth-order. To eliminate some of the numerical stiffness, we must use at least a semi-implicit time-stepping approach. It is not necessary that the resulting system is linear, since the nonlinear multigrid solver can handle nonlinearities and non-constant-coefficient linear terms in a straightforward manner. Determining which terms to treat implicitly is a balance between experience and trial and error. We propose the following time-discrete, space-continuous scheme of (2.10)–(2.13)

$$\phi^{k+1} - \phi^k = -sM_{\phi}\mu^{k+1}, \tag{3.1}$$

$$\mu^{k+1} = \gamma_1\omega^{k+1} + \gamma_2\left(\frac{\omega^{k+1}}{\varepsilon^2}g''\left(\phi^k\right) - \Delta\omega^{k+1}\right) + \gamma_3\left(B^k - A\right)\omega^{k+1} + \frac{p'\left(\phi^k\right)}{2}\left[f^{\text{in}}\left(\psi^k\right) - f^{\text{out}}\left(\psi^k\right)\right], \tag{3.2}$$

$$\omega^{k+1} = \frac{1}{\varepsilon} g'(\phi^{k+1}) - \varepsilon \Delta \phi^{k+1}, \tag{3.3}$$

$$\psi^{k+1} - \psi^k = s\nabla \cdot \left(M_{\psi}(\phi^k) \nabla v^{k+1} \right), \tag{3.4}$$

$$v^{k+1} = \frac{1 + p\left(\phi^{k}\right)}{2} \frac{df^{\text{in}}}{d\psi} \left(\psi^{k+1}\right) + \frac{1 - p\left(\phi^{k}\right)}{2} \frac{df^{\text{out}}}{d\psi} \left(\psi^{k+1}\right), \tag{3.5}$$



97 Page 10 of 31 X. Tang et al.

where s is the time step, $\gamma_1 = \gamma_{\text{surf}} \cdot \frac{3\sqrt{2}}{4}$, $\gamma_2 = \gamma_{\text{bend}} \cdot \frac{3\sqrt{2}}{8}$, $\gamma_3 = \gamma_{\text{area}} \frac{3\sqrt{2}}{4}$, $B^k = \int_{\Omega} f^{\text{surf}} \left(\phi^k, \nabla \phi^k\right) dx$, and $\partial_n \phi^{k+1} = \partial_n \mu^{k+1} = \partial_n \omega^{k+1} = \partial_n \psi^{k+1} = \partial_n \nu^{k+1} = 0$ on $\partial \Omega$.

3.2 Discretization of two-dimensional space

3.2.1 Notation and definitions

Here we follow the notation and definitions of grid functions and difference operators used in Wise (2010). Consider $\Omega = (0, L_x) \times (0, L_y) \subset \mathbb{R}^2$, with $L_x = m \cdot h$, $L_y = n \cdot h$, where h > 0 is the spatial resolution and m, n are positive integers. First, let us define

$$C_m = \left\{ \left(i - \frac{1}{2} \right) \cdot h \mid i = 1, \dots, m \right\},$$
 (3.6)

$$C_{\bar{m}} = \left\{ \left(i - \frac{1}{2} \right) \cdot h \mid i = 0, \dots, m + 1 \right\},$$
 (3.7)

$$E_m = \{i \cdot h \mid i = 0, \dots, m\}.$$
 (3.8)

 C_m and $C_{\bar{m}}$ are sets of *cell-centered points* of the interval $[0, L_x]$. E_m is a set of *edge-centered points* of $[0, L_x]$. Analogously, C_n and $C_{\bar{n}}$ contain the cell-centered points of $[0, L_y]$, and E_n is a uniform partition of $[0, L_y]$ of size n. We will consider cell-centered points as the domain of our discretized functions. We define the function spaces

$$C_{m \times n} = \{ \phi : C_m \times C_n \to \mathbb{R} \}, \qquad C_{\bar{m} \times \bar{n}} = \{ \phi : C_{\bar{m}} \times C_{\bar{n}} \to \mathbb{R} \}, \qquad (3.9)$$

$$C_{\bar{m}\times n} = \{\phi : C_{\bar{m}} \times C_n \to \mathbb{R}\}, \qquad C_{m\times \bar{n}} = \{\phi : C_m \times C_{\bar{n}} \to \mathbb{R}\}, \qquad (3.10)$$

$$\mathcal{E}_{m\times n}^{\text{ew}} = \{ f : E_m \times C_n \to \mathbb{R} \}, \qquad \mathcal{E}_{m\times n}^{\text{ns}} = \{ f : C_m \times E_n \to \mathbb{R} \}. \tag{3.11}$$

The functions of $\mathcal{C}_{m \times n}$, $\mathcal{C}_{\bar{m} \times \bar{n}}$, $\mathcal{C}_{\bar{m} \times n}$, and $\mathcal{C}_{m \times \bar{n}}$ are called *cell-centered functions*. In component form these functions are identified via $\phi_{i,j} := \phi\left(x_i, y_j\right)$, where $x_i = \left(i - \frac{1}{2}\right) \cdot h$, $y_j = \left(j - \frac{1}{2}\right) \cdot h$, and i and j are integers. The functions of $\mathcal{E}_{m \times n}^{\mathrm{ew}}$ and $\mathcal{E}_{m \times n}^{\mathrm{ns}}$ are called *east-west edge-centered functions* and *north-south edge-centered* functions, respectively. In component form east-west edge-centered functions are identified via $f_{i+\frac{1}{2},j} := f\left(x_{i+\frac{1}{2}},y_j\right)$, and north-south edge-centered functions are identified via $f_{i,j+\frac{1}{2}} := f\left(x_i,y_{j+\frac{1}{2}}\right)$, where $x_{i+\frac{1}{2}} = i \cdot h$, $y_j = \left(j - \frac{1}{2}\right) \cdot h$, $x_i = \left(i - \frac{1}{2}\right) \cdot h$, $y_{j+\frac{1}{2}} = j \cdot h$, and i and j are integers. Similarly, we define the edge-to-center difference operators $d_x : \mathcal{E}_{m \times n}^{\mathrm{ew}} \to \mathcal{C}_{m \times n}$ and $d_y : \mathcal{E}_{m \times n}^{\mathrm{ns}} \to \mathcal{C}_{m \times n}$ component-wise via

$$d_{x} f_{i,j} = \frac{1}{h} \left(f_{i+\frac{1}{2},j} - f_{i-\frac{1}{2},j} \right), \quad d_{y} f_{i,j} = \frac{1}{h} \left(f_{i,j+\frac{1}{2}} - f_{i,j-\frac{1}{2}} \right),$$

$$i = 1, \dots, m, \quad j = 1, \dots, n.$$
(3.12)



The x-dimension center-to-edge average and difference operators, respectively, A_x , D_x : $\mathcal{C}_{\bar{m}\times n} \to \mathcal{E}_{m\times n}^{\mathrm{ew}}$ are defined component-wise as

$$A_{x}\phi_{i+\frac{1}{2},j} = \frac{1}{2} \left(\phi_{i,j} + \phi_{i+1,j} \right), \quad D_{x}\phi_{i+\frac{1}{2},j} = \frac{1}{h} \left(\phi_{i+1,j} - \phi_{i,j} \right),$$

$$i = 0, \dots, m, \quad j = 1, \dots, n. \tag{3.13}$$

Likewise, the y-dimension center-to-edge average and difference operators, respectively, A_y , D_y : $\mathcal{C}_{m \times \bar{n}} \to \mathcal{E}_{m \times n}^{\mathrm{ns}}$ are defined component-wise as

$$A_{y}\phi_{i,j+\frac{1}{2}} = \frac{1}{2} \left(\phi_{i,j} + \phi_{i,j+1} \right), \quad D_{y}\phi_{i,j+\frac{1}{2}} = \frac{1}{h} \left(\phi_{i,j+1} - \phi_{i,j} \right),$$

$$i = 1, \dots, m, \quad j = 0, \dots, n.$$
(3.14)

The standard 2D discrete Laplacian, $\Delta_h: \mathcal{C}_{\bar{m}\times\bar{n}} \to \mathcal{C}_{m\times n}$, is defined as

$$\Delta_{h}\phi_{i,j} = d_{x} (D_{x}\phi)_{i,j} + d_{y} (D_{y}\phi_{i,j})$$

$$= \frac{1}{h^{2}} (\phi_{i+1,j} + \phi_{i-1,j} + \phi_{i,j+1} + \phi_{i,j-1} - 4\phi_{i,j}),$$

$$i = 1, \dots, m, \quad j = 1, \dots, n.$$
(3.15)

The spatial approximation of the 2D surface energy B^k in (3.2) is denoted B_h^k : $\mathcal{C}_{m \times n} \to \mathbb{R}$ and is defined as

$$B_{h}^{k} := h^{2} \sum_{i=1}^{m} \sum_{j=1}^{n} \frac{3\sqrt{2}}{4} \left\{ \frac{1}{\varepsilon} g(\phi_{i,j}) + \frac{\varepsilon}{2} \left[\frac{\left(D_{x} \phi_{i+\frac{1}{2},j}^{k}\right)^{2} + \left(D_{x} \phi_{i-\frac{1}{2},j}^{k}\right)^{2}}{2} + \left(D_{y} \phi_{i,j+\frac{1}{2}}^{k}\right)^{2} + \left(D_{y} \phi_{i,j-\frac{1}{2}}^{k}\right)^{2} \right\}$$

$$+ \frac{\left(D_{y} \phi_{i,j+\frac{1}{2}}^{k}\right)^{2} + \left(D_{y} \phi_{i,j-\frac{1}{2}}^{k}\right)^{2}}{2} \left\{ \right\}.$$

$$(3.16)$$

The spatial approximation of A in (3.2) is denoted A_h and is defined as $A_h := B_h^0$.

3.2.2 Boundary conditions

In this paper, we use grid functions satisfying homogeneous Neumann boundary conditions on Ω , that is, the cell-centered function $\phi \in \mathcal{C}_{\bar{m} \times \bar{n}}$ satisfies

$$\phi_{0,j} = \phi_{1,j}, \quad \phi_{m+1,j} = \phi_{m,j}, \quad j = 1, \dots, n,
\phi_{i,0} = \phi_{i,1}, \quad \phi_{i,n+1} = \phi_{i,n}, \quad i = 0, \dots, m+1,$$
(3.17)

we use the notation $\mathbf{n} \cdot \nabla_h \phi = 0$ to indicate that ϕ satisfies (3.17). Periodic boundary conditions could be used as well.



97 Page 12 of 31 X. Tang et al.

3.2.3 Fully-discrete scheme

With the notation defined above, the fully-discrete scheme for the Eqs. (3.1)–(3.5) is: given ϕ^k , $\psi^k \in \mathcal{C}_{\bar{m} \times \bar{n}}$, find the grid functions ϕ^{k+1} , μ^{k+1} , ω^{k+1} , ψ^{k+1} , $\nu^{k+1} \in \mathcal{C}_{\bar{m} \times \bar{n}}$ such that $\mathbf{n} \cdot \nabla_h \phi^{k+1} = \mathbf{n} \cdot \nabla_h \mu^{k+1} = \mathbf{n} \cdot \nabla_h \omega^{k+1} = \mathbf{n} \cdot \nabla_h \psi^{k+1} = \mathbf{n}$, and

$$\phi^{k+1} - \phi^k = -sM_{\phi}\mu^{k+1}, \qquad (3.18)$$

$$\mu^{k+1} = \gamma_1\omega^{k+1} + \gamma_2\left(\frac{\omega^{k+1}}{\varepsilon^2}g''\left(\phi^k\right) - \Delta_h\omega^{k+1}\right) + \gamma_3\left(B_h^k - A_h\right)\omega^{k+1} + \frac{p'\left(\phi^k\right)}{2}\left[f^{\text{in}}\left(\psi^k\right) - f^{\text{out}}\left(\psi^k\right)\right], \qquad (3.19)$$

$$\omega^{k+1} = \frac{1}{\varepsilon} g'(\phi^{k+1}) - \varepsilon \Delta_h \phi^{k+1}, \tag{3.20}$$

$$\psi^{k+1} - \psi^k = s \left\{ d_x \left(M_{\psi} \left(A_x \phi^k \right) D_x v^{k+1} \right) + d_y \left(M_{\psi} \left(A_y \phi^k \right) D_y v^{k+1} \right) \right\}, \tag{3.21}$$

$$v^{k+1} = \frac{1 + p\left(\phi^{k}\right)}{2} \frac{df^{\text{in}}}{d\psi} \left(\psi^{k+1}\right) + \frac{1 - p\left(\phi^{k}\right)}{2} \frac{df^{\text{out}}}{d\psi} \left(\psi^{k+1}\right). \tag{3.22}$$

3.3 Multigrid solver

We now rewrite (3.18)–(3.22) as the following component form: find ϕ^{k+1} , μ^{k+1} , ω^{k+1} , ψ^{k+1} , and ν^{k+1} in $C_{\bar{m}\times\bar{n}}$ with boundary conditions $\mathbf{n}\cdot\nabla_h\phi^{k+1}=\mathbf{n}\cdot\nabla_h\mu^{k+1}=\mathbf{n}\cdot\nabla_h\mu^{k+1}=\mathbf{n}\cdot\nabla_h\psi^{k+1}=\mathbf{n$

$$\phi_{i,j}^{k+1} + sM_{\phi}\mu_{i,j}^{k+1} = \phi_{i,j}^{k},$$

$$\mu_{i,j}^{k+1} - \left[\gamma_{1} + \frac{\gamma_{2}}{\varepsilon^{2}}g''\left(\phi_{i,j}^{k}\right) + \gamma_{3}\left(B_{h}^{k} - A_{h}\right)\right]\omega_{i,j}^{k+1} + \gamma_{2}\Delta_{h}\omega_{i,j}^{k+1}$$
(3.23)

$$=\frac{p'\left(\phi_{i,j}^{k}\right)}{2}\left[f^{\text{in}}\left(\psi_{i,j}^{k}\right)-f^{\text{out}}\left(\psi_{i,j}^{k}\right)\right],\tag{3.24}$$

$$\omega_{i,j}^{k+1} - \frac{1}{\varepsilon} \left(\left(\phi_{i,j}^{k+1} \right)^3 - \phi_{i,j}^{k+1} \right) + \varepsilon \Delta_h \phi_{i,j}^{k+1} = 0, \tag{3.25}$$

$$\psi_{i,j}^{k+1} - sd_x \left(M_{\psi} \left(A_x \phi^k \right) D_x v^{k+1} \right)_{i,j} - sd_y \left(M_{\psi} \left(A_y \phi^k \right) D_y v^{k+1} \right)_{i,j} = \psi_{i,j}^k,$$
(3.26)

$$\nu_{i,j}^{k+1} - \left[\frac{1 + p\left(\phi_{i,j}^{k}\right)}{2} \cdot \gamma_{\text{in}} + \frac{1 - p\left(\phi_{i,j}^{k}\right)}{2} \cdot \gamma_{\text{out}} \right] \psi_{i,j}^{k+1}$$

$$= -\frac{1 + p\left(\phi_{i,j}^{k}\right)}{2} \gamma_{\text{in}} \psi_{\text{in}} - \frac{1 - p\left(\phi_{i,j}^{k}\right)}{2} \gamma_{\text{out}} \psi_{\text{out}}.$$
(3.27)



Let $\phi = (\phi, \mu, \omega, \psi, \nu)^T$, define the $5 \times m \times n$ nonlinear operator $\mathbf{N} = (N^{(1)}, N^{(2)}, N^{(3)}, N^{(4)}, N^{(5)})$ as

$$N_{i,j}^{(1)} = \phi_{i,j}^{k+1} + sM_{\phi}\mu_{i,j}^{k+1}, \tag{3.28}$$

$$N_{i,j}^{(2)} = \mu_{i,j}^{k+1} - \left[\gamma_1 + \frac{\gamma_2}{\varepsilon^2} g'' \left(\phi_{i,j}^k \right) + \gamma_3 \left(B_h^k - A_h \right) \right] \omega_{i,j}^{k+1} + \gamma_2 \Delta_h \omega_{i,j}^{k+1}, \quad (3.29)$$

$$N_{i,j}^{(3)} = \omega_{i,j}^{k+1} - \frac{1}{\varepsilon} \left(\left(\phi_{i,j}^{k+1} \right)^3 - \phi_{i,j}^{k+1} \right) + \varepsilon \Delta_h \phi_{i,j}^{k+1}, \tag{3.30}$$

$$N_{i,j}^{(4)} = \psi_{i,j}^{k+1} - s d_x \left(M_{\psi} \left(A_x \phi^k \right) D_x v^{k+1} \right)_{i,j} - s d_y \left(M_{\psi} \left(A_y \phi^k \right) D_y v^{k+1} \right)_{i,j},$$
(3.31)

$$N_{i,j}^{(5)} = \nu_{i,j}^{k+1} - \left[\frac{1 + p\left(\phi_{i,j}^{k}\right)}{2} \cdot \gamma_{\text{in}} + \frac{1 - p\left(\phi_{i,j}^{k}\right)}{2} \cdot \gamma_{\text{out}} \right] \psi_{i,j}^{k+1}, \tag{3.32}$$

and the $5 \times m \times n$ source $\mathbf{S} = (S^{(1)}, S^{(2)}, S^{(3)}, S^{(4)}, S^{(5)})$ as

$$S_{i,j}^{(1)} = \phi_{i,j}^k, \tag{3.33}$$

$$S_{i,j}^{(2)} = \frac{p'\left(\phi_{i,j}^k\right)}{2} \left[f^{\text{in}}\left(\psi_{i,j}^k\right) - f^{\text{out}}\left(\psi_{i,j}^k\right) \right], \tag{3.34}$$

$$S_{i,j}^{(3)} = 0, (3.35)$$

$$S_{i,j}^{(4)} = \psi_{i,j}^k, \tag{3.36}$$

$$S_{i,j}^{(5)} = -\frac{1 + p\left(\phi_{i,j}^{k}\right)}{2} \gamma_{\text{in}} \psi_{\text{in}} - \frac{1 - p\left(\phi_{i,j}^{k}\right)}{2} \gamma_{\text{out}} \psi_{\text{out}}.$$
 (3.37)

Then, the system (3.23)–(3.27) is equivalent to $\mathbf{N}(\boldsymbol{\phi}^{k+1}) = \mathbf{S}(\boldsymbol{\phi}^k)$.

Next, we apply the nonlinear FAS multigrid method to solve $\mathbf{N}(\boldsymbol{\phi}^{k+1}) = \mathbf{S}(\boldsymbol{\phi}^k)$ for a given $\boldsymbol{\phi}^k$. The main points of this method are: (1) we first need a smoothing operator for generating smoothed approximate solutions of $\mathbf{N}(\boldsymbol{\phi}) = \mathbf{S}$, here we use a nonlinear Gauss–Seidel method with Red-Black ordering; (2) we then use this smoothing operator on each hierarchical grid to get better approximation of $\boldsymbol{\phi}^{k+1}$. For further use, we represent the smoothing operator as

$$\bar{\boldsymbol{\phi}} = \text{Smooth}(\boldsymbol{\phi}, \mathbf{N}, \mathbf{S}, \lambda),$$
 (3.38)

where λ is the number of smoothing sweeps. Next, let's give the details of this operator. Here, ℓ is the index for iterative step, and we set

$$\begin{split} \phi_{i+\frac{1}{2},j}^{\text{ew}} &:= A_x \phi_{i+\frac{1}{2},j}^k, \qquad \phi_{i,j+\frac{1}{2}}^{\text{ns}} := A_y \phi_{i,j+\frac{1}{2}}^k \\ M_{\psi}_{i+\frac{1}{2},j}^{\text{ew}} &:= M_{\psi} \left(\phi_{i+\frac{1}{2},j}^{\text{ew}} \right), \ M_{\psi}_{i,j+\frac{1}{2}}^{\text{ns}} := M_{\psi} \left(\phi_{i,j+\frac{1}{2}}^{\text{ns}} \right). \end{split}$$



97 Page 14 of 31 X. Tang et al.

The Gauss–Seidel smoothing works as following: for every (i, j), stepping lexicogrphically from (1, 1) to (m, n), find $\phi_{i,j}^{\ell+1}$, $\mu_{i,j}^{\ell+1}$, $\phi_{i,j}^{\ell+1}$, $\psi_{i,j}^{\ell+1}$, and $v_{i,j}^{\ell+1}$ that solve

$$\phi_{i,j}^{\ell+1} + sM_{\phi}\mu_{i,j}^{\ell+1} = S_{i,j}^{(1)}\left(\phi^{k}\right), \tag{3.39}$$

$$\mu_{i,j}^{\ell+1} - \left[\gamma_{1} + \frac{\gamma_{2}}{\varepsilon^{2}}g''\left(\phi_{i,j}^{k}\right) + \gamma_{3}\left(B_{h}^{k} - A_{h}\right) + \frac{4\gamma_{2}}{h^{2}}\right]\omega_{i,j}^{\ell+1} = S_{i,j}^{(2)}\left(\phi^{k}\right)$$

$$- \frac{\gamma_{2}}{h^{2}}\left[\omega_{i+1,j}^{\ell} + \omega_{i-1,j}^{\ell+1} + \omega_{i,j+1}^{\ell} + \omega_{i,j-1}^{\ell+1}\right], \tag{3.40}$$

$$\omega_{i,j}^{\ell+1} - \left[\frac{1}{\varepsilon}(\phi_{i,j}^{\ell})^{2} + \frac{4\varepsilon}{h^{2}}\right]\phi_{i,j}^{\ell+1} = S_{i,j}^{(3)}\left(\phi^{k}\right) - \frac{1}{\varepsilon}\phi_{i,j}^{\ell}$$

$$- \frac{\varepsilon}{h^{2}}\left[\phi_{i+1,j}^{\ell} + \phi_{i-1,j}^{\ell+1} + \phi_{i,j+1}^{\ell} + \phi_{i,j-1}^{\ell+1}\right], \tag{3.41}$$

$$\psi_{i,j}^{\ell+1} + \frac{s}{h^{2}}\left[M_{\psi_{i+\frac{1}{2},j}} + M_{\psi_{i-\frac{1}{2},j}} + M_{\psi_{i,j+\frac{1}{2}}} + M_{\psi_{i,j-\frac{1}{2}}} \right]\nu_{i,j}^{\ell+1}$$

$$= S_{i,j}^{(4)}\left(\phi^{k}\right) + \frac{s}{h^{2}}\left[M_{\psi_{i,j+1}}^{\text{ew}} + M_{\psi_{i,j-\frac{1}{2}}} \nu_{i+1,j}^{\ell+1} + M_{\psi_{i-\frac{1}{2},j}} \nu_{i-1,j}^{\ell+1} + M_{\psi_{i,j+\frac{1}{2}}} \nu_{i,j+1}^{\ell+1} + M_{\psi_{i,j-\frac{1}{2}}} \nu_{i,j-1}^{\ell+1}\right], \tag{3.42}$$

$$\nu_{i,j}^{\ell+1} - \left[\frac{1+p\left(\phi_{i,j}^{k}\right)}{2} \cdot \gamma_{\text{in}} + \frac{1-p\left(\phi_{i,j}^{k}\right)}{2} \cdot \gamma_{\text{out}}\right]\psi_{i,j}^{\ell+1} = S_{i,j}^{(5)}\left(\phi^{k}\right). \tag{3.43}$$

In practice, we use Cramer's Rule to solve this 5×5 linear system (3.39)–(3.43) or use Cramer's Rule to solve 3×3 linear system (3.39)–(3.41) and solve 2×2 linear system (3.42)–(3.43) simultaneously, since (3.39)–(3.41) and (3.42)–(3.43) are independent.

Multigrid works on a hierarchy of grids. We use the smoothing operator on each level of the grids to get a better approximation. Here, we set minlevel \leq level \leq 0, 0 means the index of the finest grid, and minlevel is the index of the coarsest grid. We also need to transform the results between two levels of grids. By $\mathbf{I}_{\text{level}}^{\text{level-1}}$ we denote the restriction operator which is defined by cell-center averaging, and by $\mathbf{I}_{\text{level}-1}^{\text{level}}$ we denote the prolongation operator which is defined by piece-wise constant interpolation. $\mathbf{I}_{\text{level}}^{\text{level-1}}$ transfers fine grid functions to the coarse grid, while $\mathbf{I}_{\text{level}-1}^{\text{level}}$ transfers coarse grid functions to the fine grid. The following is the algorithm for our multigrid solver (Wise 2010), in which $\phi_{\text{level}}^{k+1,m+1} = \text{FASV} \text{cycle}\left(\phi_{\text{level}}^{k+1,m}, \mathbf{N}_{\text{level}}, \mathbf{S}_{\text{level}}, \lambda$, level) is the recursive FAS V-Cycle iteration operator and the superscript m is the V-Cycle loop index.

3.4 Algorithm

RECURSIVE FAS V-CYCLE OPERATOR

$$\phi_{\text{level}}^{k+1,m+1} = \text{FASVcycle}\left(\phi_{\text{level}}^{k+1,m}, \mathbf{N}_{\text{level}}, \mathbf{S}_{\text{level}}, \lambda, \text{level}\right)$$



Pre-smoothing:

$$\bar{\boldsymbol{\phi}}_{\text{level}} = \text{Smooth}\left(\boldsymbol{\phi}_{\text{level}}^{k+1,m}, \mathbf{N}_{\text{level}}, \mathbf{S}_{\text{level}}, \lambda\right)$$

Coarse-grid correction:

If level > minlevel

$$\mathbf{S}_{level-1} = \mathbf{I}_{level}^{level-1} \left(\mathbf{S}_{level} - \mathbf{N}_{level} \right) + \mathbf{N}_{level-1} \left(\mathbf{I}_{level}^{level-1} \bar{\boldsymbol{\phi}}_{level} \right), \tag{3.44}$$

$$\mathbf{\bar{\phi}}_{level-1} = FASV cycle\left(\mathbf{I}_{level}^{level-1} \boldsymbol{\phi}_{level}, \mathbf{N}_{level-1}, \mathbf{S}_{level-1}, \lambda, level-1\right), \quad (3.45)$$

$$\hat{\boldsymbol{\phi}}_{\text{level}-1} = \bar{\boldsymbol{\phi}}_{\text{level}-1} - \mathbf{I}_{\text{level}}^{\text{level}-1} \bar{\boldsymbol{\phi}}_{\text{level}}, \tag{3.46}$$

$$\hat{\phi}_{\text{level}} = \bar{\phi}_{\text{level}} + I_{\text{level-1}}^{\text{level}} \hat{\phi}_{\text{level-1}}, \tag{3.47}$$

post-smooth:
$$\phi_{\text{level}}^{k+1,m+1} = \text{Smooth}\left(\hat{\phi}_{\text{level}}, \mathbf{N}_{\text{level}}, \mathbf{S}_{\text{level}}, \lambda\right).$$
 (3.48)

end if

The combined algorithm of time stepping and the FAS V-Cycle iteration operator is given as follows.

COMBINED TIME STEPPING AND FAS V-CYCLE ITERATION ALGORITHM

Initialize
$$\phi_0^{k=0}$$
 Time Step Loop: for $k=0$, $k_{\max}-1$ set $\phi_0^{k+1,m=0}=\phi_0^k$ calculate $\mathbf{S}_0\left(\phi_0^k\right)$ V-cycle Loop: for $m=0$, $m_{\max}-1$ $\phi_0^{k+1,m+1}=\mathrm{FASV}$ cycle $\left(\phi_0^{k+1,m},\mathbf{N}_0,\mathbf{S}_0,\lambda,0\right)$ if $\left\|\mathbf{S}_0\left(\phi_0^{k+1,m+1}\right)-\mathbf{N}_0\left(\phi_0^{k+1,m+1}\right)\right\|_{2,\star}<\tau$, then set $\phi_0^{k+1}=\phi_0^{k+1,m+1}$ and exit V-cycle Loop end for V-cycle Loop end for Time Step Loop

Here $\tau > 0$ is the stopping tolerance, and the norm is defined by

$$\|\mathbf{R}(\boldsymbol{\phi})\|_{2,*} := \sqrt{\frac{1}{5mn} \sum_{k=1}^{5} \sum_{i=1}^{m} \sum_{j=1}^{n} \left(R_{i,j}^{(k)}(\boldsymbol{\phi}) \right)^{2}},$$
 (3.49)

where $\mathbf{R}(\phi) := \mathbf{S}(\phi^k) - \mathbf{N}(\phi)$ is the $5 \times m \times n$ residual array, and $R_{i,j}^{(k)}(\phi)$ are its components.



97 Page 16 of 31 X. Tang et al.

4 Numerical results

In this section, we discuss numerical results of the discrete system (3.18)–(3.22) solved by the nonlinear FAS multigrid algorithm. We present the results of convergence tests and perform sample computations. In all the tests below, we set $L_x = L_y$ for simplicity, and use the interpolation function $p(\phi) = -\frac{1}{2}\phi^3 + \frac{3}{2}\phi$, which satisfies p(1) = 1, p(-1) = -1, and p'(-1) = p'(1) = 0 in (2.3). In the first set of tests in Sect. 4.1, we show evidence that the multigrid solver converges with optimal (or near optimal) complexity. In the second set of tests in Sect. 4.2, we provide evidence that the scheme is convergent and the global error is of first order in time and second order in space. We then present a series numerical studies on the growth and shrinkage cases using the condition established in Sect. 2.2.

4.1 Convergence and complexity of the multigrid solver

that the optimal value of λ should be less than 5.

We perform six separate tests to demonstrate the convergence and near optimal complexity (with respect to the grid size h) of the multigrid solver. We provide evidence that the multigrid convergence rate is nearly independent of h. For all the tests we take the initial data

$$\phi_{i,j}^{0} = \tanh\left(\frac{0.18 - \sqrt{0.75(x_i - 0.5)^2 + (y_j - 0.5)^2}}{\sqrt{2}\varepsilon}\right),\tag{4.1}$$

$$\psi_{i,j}^{0} = -\phi_{i,j}^{0} \times 0.1 + 0.7, \tag{4.2}$$

and set the parameters $L_x = L_y = 1.0$, $\gamma_{\text{surf}} = 1.0$, $\gamma_{\text{area}} = 1.0 \times 10^4$, $\gamma_{\text{in}} = 1.0 \times 10^5$, $\gamma_{\text{out}} = 1.0 \times 10^5$, $\gamma_{\text{out}} = 0.1$, $\gamma_{\text{out}} = 0.8$, $\gamma_{\text{out}} = 0.5$, $\gamma_{\text{out}} = 0.0$, $\gamma_{\text{out}} = 0.0$. We use the temporal step size $\gamma_{\text{out}} = 0.0$, $\gamma_{\text{out}} = 0.0$, $\gamma_{\text{out}} = 0.0$. We use the temporal step size $\gamma_{\text{out}} = 0.0$, and study the numerical results at the 20th time step. We vary the spatial step size $\gamma_{\text{out}} = 0.0$, $\gamma_{\text{out}} = 0.$

In Table 1, we show the number of multigrid iterations needed for various choices of ε , λ , and γ_{bend} . We can see that for the smoothing parameter $\lambda=2$, the required number of iterations is nearly independent of h. The detailed residual values for Test 2 and Test 6 in Table 1 are given in graphical form in Fig. 5, from which we observe for $\lambda=2$ the norm of residual is reduced approximately the same factor at each iteration regardless of h. With $\lambda=1$, we do not have this. By these features of multigrid operator with optimal complexity in Kay and Welford (2006), Trottenberg et al. (2001), it is evident that the multigrid solver here has near optimal complexity at $\lambda=2$.



Table 1 The number of multigrid iterations required to reduce the norm of the residual below the tolerance $au=1.0 imes10^{-8}$

	Test 1	Test 2	Test 3	Test 4	Test 5	Test 6	Test 7	Test 8
હ	2×10^{-2}	2×10^{-2}	3×10^{-2}	5×10^{-2}	2×10^{-2}	2×10^{-2}	3×10^{-2}	5×10^{-2}
γ	1	-	1	1	2	2	2	2
	0.1	-	0.5	1	0.1	1	0.5	-
h								
1.0/128	111	6	8	11	8	8	10	7
1.0/256	111	10	6	11	8	6	6	7
1.0/512	10	11	10	12	6	6	6	8
1.0/1024	111	12	11	12	6	6	6	∞

The data are checked at the 20th time step using the fixed temporal step size $s = 5.0 \times 10^{-7}$. The initial data are given by (4.1)–(4.2). The parameters are given in the text and in the table. The precise residual values for Test 2 and 6 are shown in Fig. 5. Using the multigrid smoothing parameter $\lambda = 2$ we observe, for a variety of parameter sets, that the required number of iterations is nearly independent of h



97 Page 18 of 31 X. Tang et al.

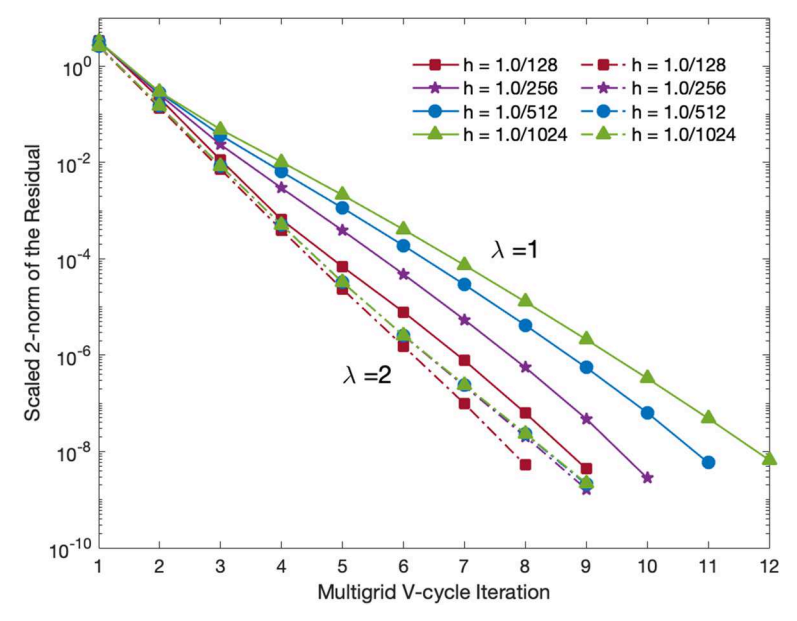


Fig. 5 The residual values per multigrid iteration in Test 2 and 6 at the 20th time step with step size $s = 5.0 \times 10^{-7}$. The initial data are given by (4.1)–(4.2). The parameters are given in the text and in Table 1. The results show that the residual reduction is nearly independent of h at $\lambda = 2$, which suggests the near optimal complexity of the solver

4.2 Convergence of the scheme as s, $h \rightarrow 0$

Next, we perform convergence tests of our scheme (3.18)–(3.22) as $s,h \to 0$. We expect that, at best, the global error in ϕ is $e_{t=T} = \mathcal{O}(s) + \mathcal{O}(h^2)$. To this end, we perform four tests similar to those in Wise (2010), under the same conditions except a refinement path of the form $s = Ch^2$. The initial data is given in (4.1)–(4.2) and the parameters used are $L_x = L_y = 1.0$; $\varepsilon = 0.02$; $\gamma_{\text{bend}} = 0.1$; $\gamma_{\text{surf}} = 1.0$; $\gamma_{\text{area}} = 1.0 \times 10^4$; $\gamma_{\text{in}} = 1.0 \times 10^5$; $\gamma_{\text{out}} = 1.0 \times 10^5$; $\gamma_{\text{out}} = 0.1$; $\gamma_{\text{out}} =$

4.3 Vesicle growth

In this section, we show the effect that the interior region of vesicle will expand, while the arclength (surface area in 3D) remain roughly a constant. We use initial conditions



Table 2 Errors and convergence rates of the scheme (3.18)–(3.22)

Grid sizes	128 ² -256 ²		256 ² -512 ²		512 ² -1024 ²
Error	1.09×10^{-2}		2.87×10^{-3}		7.25×10^{-4}
Rate		1.93		1.98	

Parameters are given in the text and the initial data is given by (4.1)–(4.2). Four tests with a refinement step size $s = Ch^2$ are presented. The error here is the global error between two nearby tests. The rate here suggests second order convergence rate in h is attained, i.e., $e = \mathcal{O}(h^2)$

and parameters as the growth case described in Sect. 2.2. We take the initial condition $\phi^0_{i,j}$ by evolving the initial data $\hat{\phi}^0_{i,j}$ a few time steps using the classical Cahn–Hilliard equation:

$$\hat{\phi}_{i,j}^0 = 1$$
, if $(x_i, y_j) \in \Omega_1 = \{(x_i, y_j) | (x_i - 0.5)^2 + (y_j - 0.5)^2 \le r^2 \}$ (4.3)

$$\hat{\phi}_{i,j}^0 = -1, \quad \text{if} \quad (x_i, y_j) \in \Omega \backslash \Omega_1 \tag{4.4}$$

and

$$\psi_{i,j}^{0} = -\phi_{i,j}^{0} \times 0.35 + 0.45, \quad (x_i, y_j) \in \Omega$$
 (4.5)

where $r = 0.18 + 0.03\cos(10\theta)$ and $\theta \in [0, 2\pi]$. We use parameters $L_x = L_y = 1.0$; h = 1.0/256; $\varepsilon = 0.01$; $\gamma_{\text{surf}} = 1.0$; $\gamma_{\text{bend}} = 0.05$; $\gamma_{\text{area}} = 5.0 \times 10^4$; $\gamma_{\text{in}} = 1.0 \times 10^5$; $\gamma_{\text{out}} = 1.0 \times 10^5$; $\gamma_{\text{out}} = 0.0$; $\gamma_{\text{ou$

The initial concentration of the outer phase is $\psi^0 = 0.8 = \psi_\star^{\rm out}$, which is at the equilibrium value. For the inner phase, the initial concentration is $\psi^0 = 0.1$. We next perform two sample computations with the equilibrium concentration of the inner phase $\psi_\star^{\rm in} = 0.3$ or $\psi_\star^{\rm in} = 0.65$. According to the common tangent analysis in Sect. 2.2, both cases will experience growth.

In Figs. 6 and 7, we show the result when $\psi_{\star}^{\rm in}=0.3$ and $\psi_{\star}^{\rm in}=0.65$, respectively. In both calculations, we can see the growth of inner regions from the shape evolution (the evolution of ϕ) in (a) of the two figures. The difference is that the vesicle in Fig. 7 grows into a circle, which is the state with maximized volume when the interface area stay unchanged; while the one in Fig. 6 does not. Data in (b)–(e) of both figures explain how these changes and differences happen. (b) shows the evolution of energy $F^{\rm surf}$, $F^{\rm bend}$, $F^{\rm area}$, and $F^{\rm osm}$, respectively. It's easy to see that the total energy drops significantly, mainly due to the rapid decline of $F^{\rm osm}$, while the surface energy, $F^{\rm surf}$, remains roughly constant because of the penalty coefficient $\gamma_{\rm area}$. The detailed data relevant to $F^{\rm surf}$, specifically, the arclength of the interface, are shown in (c). We note that both changes are within 4×10^{-3} , that is within 0.265% compared to the original value. (d) shows the mass changes in the domain Ω , the interior region (white), and the exterior region (black), respectively. The interior mass grows with the same amount that is lost in the exterior region, i.e. the total mass is conserved. (e) shows the evolution of concentration of the interior region ($\psi^{\rm in}$) and the concentration of the exterior region



97 Page 20 of 31 X. Tang et al.

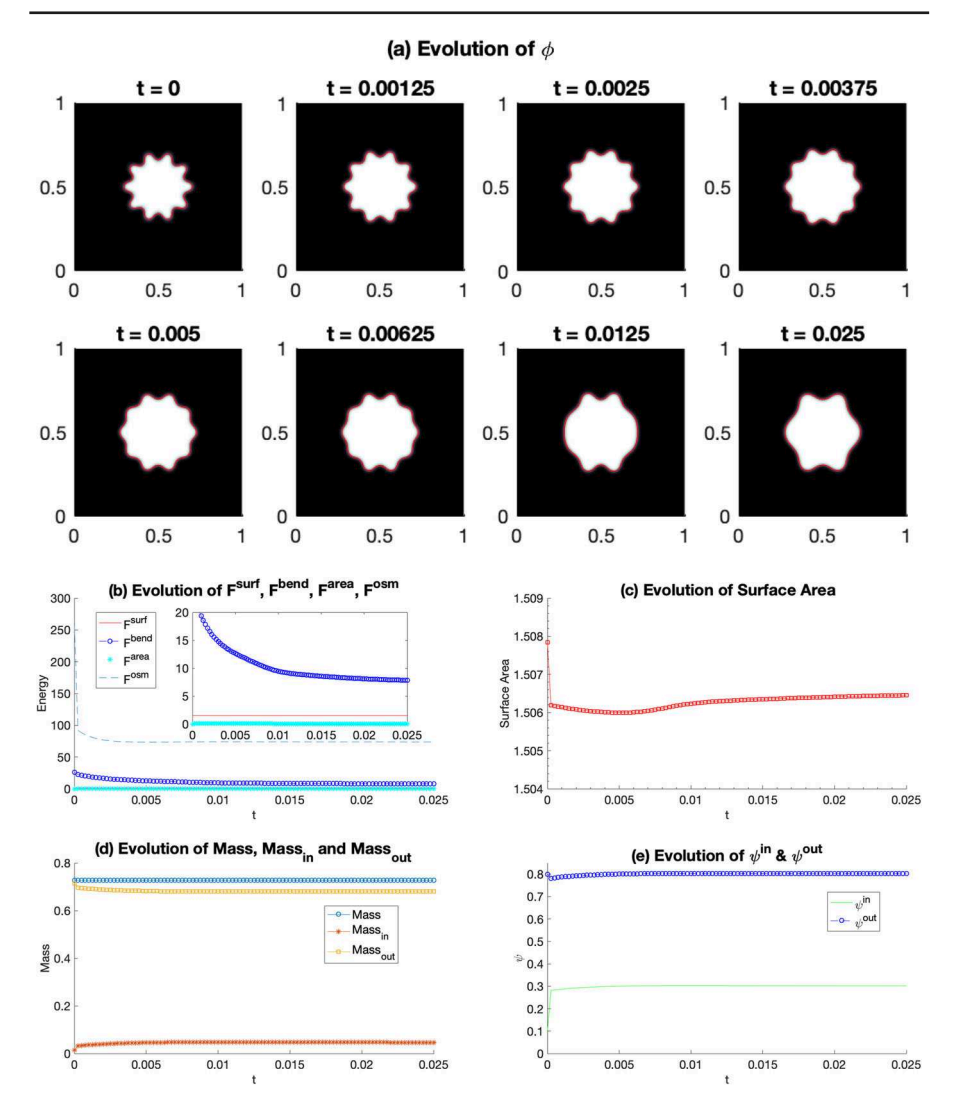


Fig. 6 The evolution of ϕ , energy, surface area, mass, and concentration in a growth case. The initial condition is given in (4.3)–(4.5) and the parameters are in the text. The only initial difference with Fig. 7 is that here we set $\psi_{\star}^{\rm in}=0.3$. In **a**, it shows the growth of inner region. The wrinkled interface stretches gradually with permanent area. In **b**, the osmotic energy declines rapidly causing the interior growth. The bending energy drops during the swelling. The surface energy remain roughly a constant and $F^{\rm area}$ stay close to 0 due to the penalty coefficient $\gamma_{\rm area}$. In **c**, it presents the change of $F^{\rm surf}$, i.e., the interface area, is within 2×10^{-3} , 0.133% compared to the original surface area. In **d**, the interior mass grows with the same amount lost in the exterior region, i.e., the total mass is conserved. In **e**, it shows that $\psi^{\rm in}$ increases to the equilibrium value $\psi_{\star}^{\rm in}=0.3$, while $\psi^{\rm out}$ stays at the value of equilibrium $\psi_{\star}^{\rm out}=0.8$



 (ψ^{out}) . Curves in Fig. 6e present that ψ^{in} increases to its equilibrium value $\psi^{\mathrm{in}}_{\star}=0.3$ and ψ^{out} stays at the equilibrium value $\psi^{\mathrm{out}}_{\star}=0.8$, which is consistent with the analysis in Sect. 2.2.

In Fig. 7, the simulation results are different. The reason is that a significant amount of net mass must be moved from the outer phase into the inner phase to attain the equilibrium value $\psi_{\star}^{\rm in}=0.65$ in the inner phase. However, the arclength inextensibility here does not allow the inner concentration to increase to the expected equilibrium value 0.65, because the vesicle already reaches a circular morphology, the shape with the maximum area (volume in 3D) for the fixed arclength, and cannot accept any additional mass from the exterior region.

For the same initial condition in (4.3)–(4.5), we now set $\gamma_{\rm bend} = 0.5$ which means a ten times bending energy $F^{\rm bend}$ compared to the previous calculation, and other parameters remain the same as those used in Fig. 7. The results are summarized in Fig. 8. Compared to Fig. 7, the shape evolution in Fig. 8 are obviously different at the first several time steps due to a much faster decline of $F^{\rm bend}$. Eventually the interface evolves into a circle.

In Fig. 9, we show shape evolution of four vesicles with different initial configurations, and other parameters remain the same as those used in Fig. 7. Numerical experiments show the following: the white region will grow with the decline of osmotic energy; the sharp corners will swell faster for a fast drop of bending energy; as long as the inner equilibrium concentration ψ_{\star}^{in} and the initial osmotic energy F^{osm} are large enough, the inner region will grow into a circle with preserved arclength.

4.4 Shrinkage simulations

In this section, we study vesicle shrinking following the condition discussed in Sect. 2.2. That is, the area of the vesicle will decrease with prescribed arclength. We take the initial condition $\phi_{i,j}^0$ by evolving the initial data $\hat{\phi}_{i,j}^0$ a few time steps using the classical Cahn-Hilliard equation:

$$\hat{\phi}_{i,j}^0 = 1$$
, if $(x_i, y_j) \in \Omega_1 = \left\{ (x_i, y_j) | (x_i - 0.5)^2 + (y_j - 0.5)^2 \le r^2 \right\}$ (4.6)

$$\hat{\phi}_{i,j}^0 = -1. \quad \text{if} \quad (x_i, y_j) \in \Omega \backslash \Omega_1 \tag{4.7}$$

and

$$\psi_{i,j}^{0} = -\phi_{i,j}^{0} \times 0.1 + 0.7, \quad (x_i, y_j) \in \Omega$$
 (4.8)

where $r = 0.3 + 0.01 \cos(10\theta)$ and $\theta \in [0, 2\pi]$. We set parameters $L_x = L_y = 1.0$; h = 1.0/256; $\varepsilon = 0.01$; $\gamma_{\text{surf}} = 1.0$; $\gamma_{\text{bend}} = 0.1$; $\gamma_{\text{area}} = 5.0 \times 10^4$; $\gamma_{\text{in}} = 1.0 \times 10^5$; $\gamma_{\text{out}} = 1.0 \times 10^5$; $\psi_{\text{in}} = 0.1$; $\psi_{\text{out}} = 0.8$; $M_0 = 0.5$; $M_\phi = 1.0$; $\beta_{\text{in}} = 0.0$; $\beta_{\text{out}} = 0.0$; $s = 1.0 \times 10^{-6}$; and the final time is $T = 4.0 \times 10^{-2}$. In this case, the equilibrium concentration values are $\psi_{\text{in}}^{\text{in}} = \psi_{\text{in}} = 0.1$ and $\psi_{\text{vul}}^{\text{out}} = \psi_{\text{out}} = 0.8$.

In Fig. 10a, we show the shape evolution of ϕ , which is obviously shrinking in area while the arclength remains roughly constant. Consequently, the interface becomes wrinkled. In Fig. 10b, we show the energy evolution curves of F^{surf} , F^{bend} , F^{area} , and



97 Page 22 of 31 X. Tang et al.

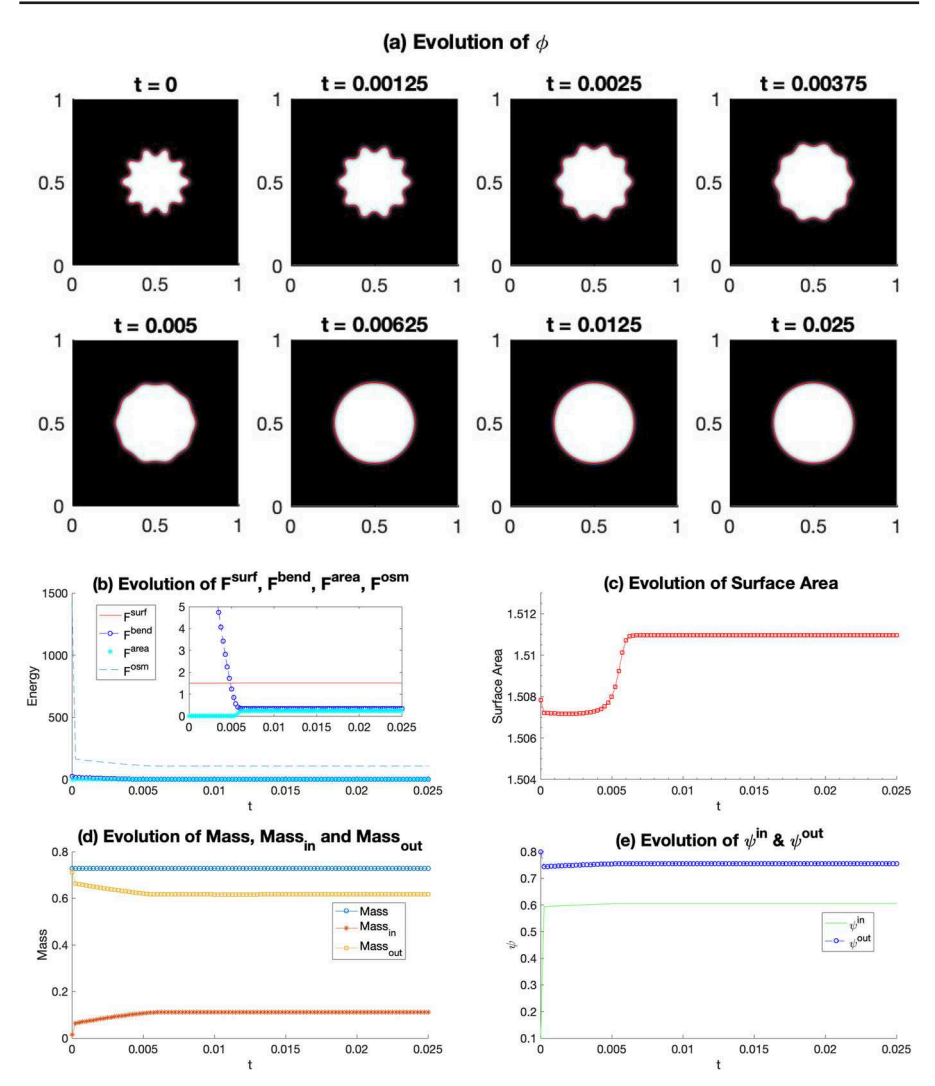


Fig. 7 The evolution of ϕ , energy, surface area, mass, and concentration in a growth case. The initial condition is given in (4.3)–(4.5) and the parameters are in the text. The only initial difference with Fig. 6 is that $\psi_*^{\text{in}} = 0.65$. In **a**, it shows the growth of inner region. The wrinkled interface stretches gradually with permanent area and eventually the vesicle grows into a circle. In **b**, the osmotic energy declines rapidly causing the interior growth. The bending energy drops until the wrinkled interface grows into a circle. The surface energy remain roughly a constant and F^{area} stay close to 0 due to the penalty coefficient γ_{area} . In **c**, it presents the change of F^{surf} , i.e., the interface area, is within 4×10^{-3} , 0.265% compared to the original surface area. In **d**, the inside mass grows with the same amount lost in the outside region, i.e., the total mass is conserved. In **e**, it shows that ψ^{in} increases toward the equilibrium value $\psi_*^{\text{in}} = 0.65$ but stays at about 0.6 while ψ^{out} stays close to but not at the value of equilibrium $\psi_*^{\text{out}} = 0.8$, because the vesicle already reaches a circular morphology (the shape with the maximum area with fixed arclength) and cannot accept any additional mass from the exterior region



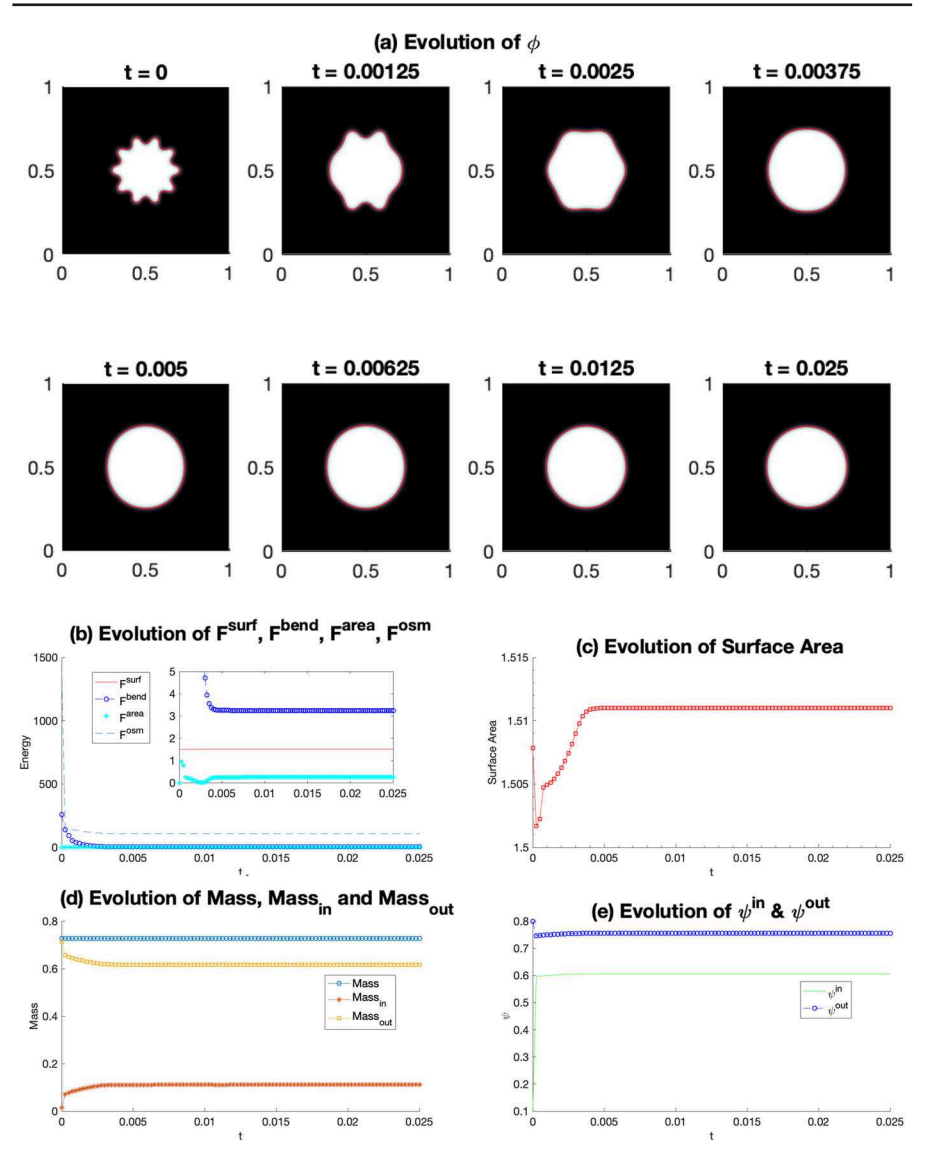


Fig. 8 The evolution of ϕ , energy, surface area, mass, and concentration for another growth case. The initial condition and the parameters are the same as those in Fig. 7 except $\gamma_{\text{bend}} = 0.5$. In **a**, it shows the similar growth effect as in Fig. 7: the wrinkled interface stretches with permanent area and finally grows into a circle. But the shapes at the first several time steps are obviously different due to a faster decline of F^{bend} . In **b**, the decline of osmotic energy causes the interior growth. The bending energy drops until the wrinkled interface grows into a circle. F^{surf} remain roughly a constant and F^{area} stay close to 0 due to the penalty coefficient γ_{area} . In **c**-**d**, it presents the surface area constraint and mass conservation. In **e**, it shows ψ^{in} approaches the equilibrium value $\psi^{\text{in}}_{\star} = 0.65$, and ψ^{out} stay close to the value of the equilibrium $\psi^{\text{out}}_{\star} = 0.8$ as in Fig. 7



97 Page 24 of 31 X. Tang et al.

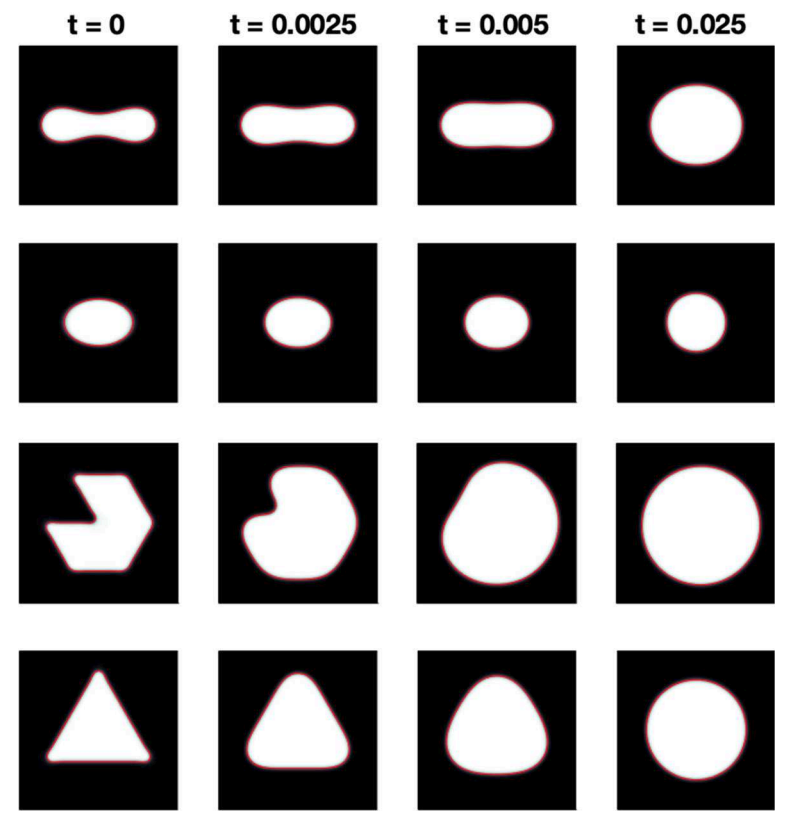


Fig. 9 Shape evolution of other growth examples with different initial conditions but same parameters as in Fig. 7. The white regions grow because of the decline of osmotic energy; the sharp corners swell faster for a fast drop of bending energy; as long as the inner equilibrium concentration ψ_{\star}^{in} and the initial osmotic energy F^{osm} are great enough, the inner region will grow into a circle with preserved surface area

 $F^{
m osm}$. $F^{
m bend}$ slightly increases at early times when $F^{
m osm}$ drop significantly, leading to a shrinkage of the vesicle volume. $F^{
m surf}$, however, stays roughly unchanged due to the arclength constraint. The detailed data of the surface area could be checked in Fig. 10c. Figure 10d gives the change of mass of the interior and exterior regions, as well as the total mass conservation. In Fig. 10e, the inner concentration $\psi^{
m in}$ is approaching the equilibrium value $\psi_{\star}^{
m in}=0.1$, while outer concentration $\psi^{
m out}$ roughly stays at the equilibrium value $\psi_{\star}^{
m out}=0.8$.

Next, we study the shape evolution when $\gamma_{bend} = 1$, which is a ten times larger bending energy compared with the previous computation. In Fig. 11, we find that the inner phase shrinks with a very different pattern due to a much larger bending energy. In particular, this change leads to the pinch-off and reattachment of bulbs which may not be biologically realistic. In other words, this parameter, γ_{bend} may be out of range relative to the other parameters. The energy changes are similar to the ones in Fig. 10b. In Fig. 11c, d, we present the surface area constraint and mass conservation.



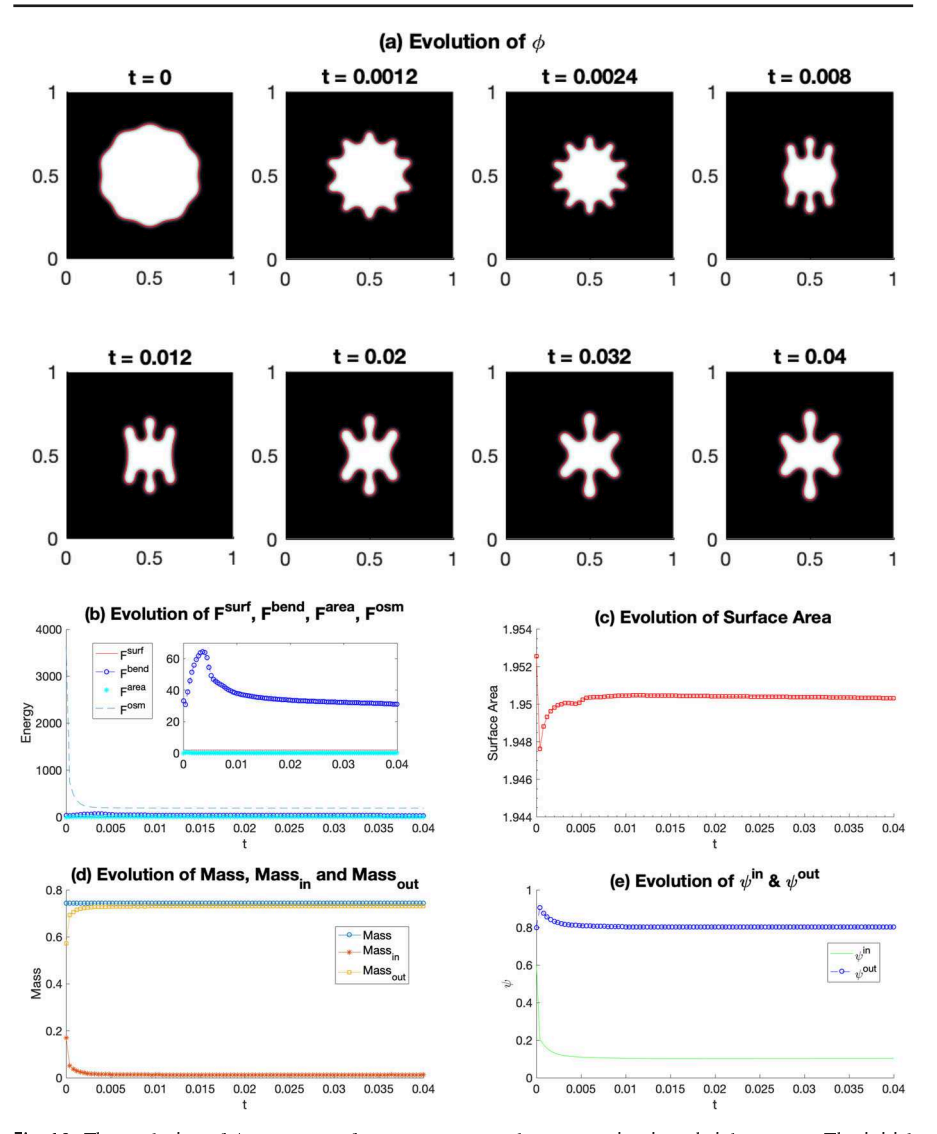


Fig. 10 The evolution of ϕ , energy, surface area, mass, and concentration in a shrinkage case. The initial condition is given in (4.6)–(4.8) and the parameters are in the text. In ${\bf a}$, it shows shrinkage effects where the interface becomes wrinkled with prescribed surface area and the sharp corners shrink to form finger-like structures. In ${\bf b}$, the osmotic energy declines rapidly causing the inner region shrinking. The bending energy slightly grows at first because of the shrinking. The surface energy remain roughly a constant and $F^{\rm area}$ stay close to 0 due to the surface area constraint. In ${\bf c}$, it presents the change of $F^{\rm surf}$ is within 5×10^{-3} , 0.26% compared to the original surface area. In ${\bf d}$, it implies the mass conservation. In ${\bf e}$, $\psi^{\rm in}$ approaches the equilibrium value $\psi^{\rm in}_{\star}=0.1$, while $\psi^{\rm out}$ stays at the equilibrium value $\psi^{\rm out}_{\star}=0.8$



97 Page 26 of 31 X. Tang et al.

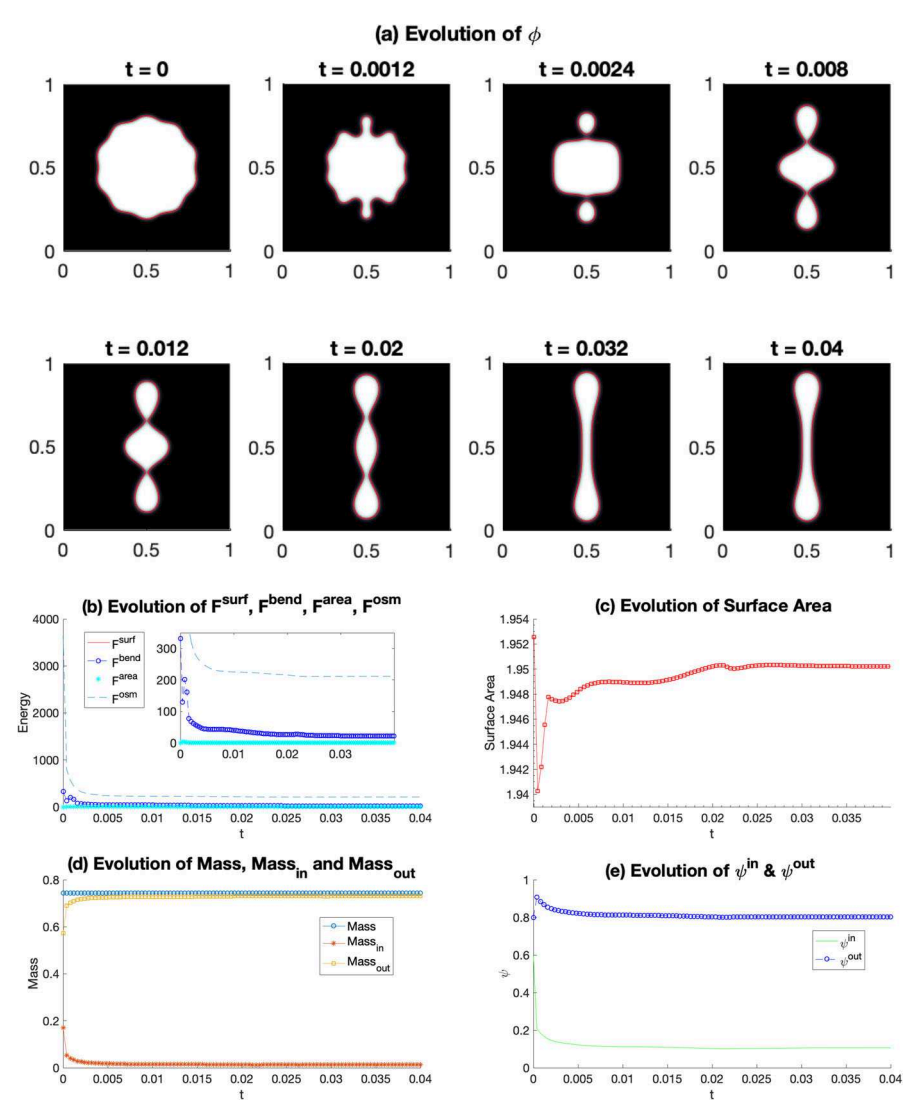


Fig. 11 The evolution of ϕ , energy, surface area, mass, and concentration in another shrinkage case. The initial condition and the parameters are the same as those in Fig. 10 except $\gamma_{\rm bend}=1$. In ${\bf a}$, it shows the similar shrinkage effect as in Fig. 10: the interface become wrinkled with permanent area, but the shape is different due to a much greater $F^{\rm bend}$. In ${\bf b}$, decline of the osmotic energy causes the inner region shrinking. $F^{\rm bend}$ decreases, $F^{\rm surf}$ remains roughly a constant and $F^{\rm area}$ stays close to 0. In ${\bf c}$ - ${\bf d}$, it presents the interface area constraint and mass conservation. In ${\bf e}$, $\psi^{\rm in}$ approaches the equilibrium value $\psi^{\rm in}_{\star}=0.1$, while $\psi^{\rm out}$ stays at the equilibrium value $\psi^{\rm out}_{\star}=0.8$



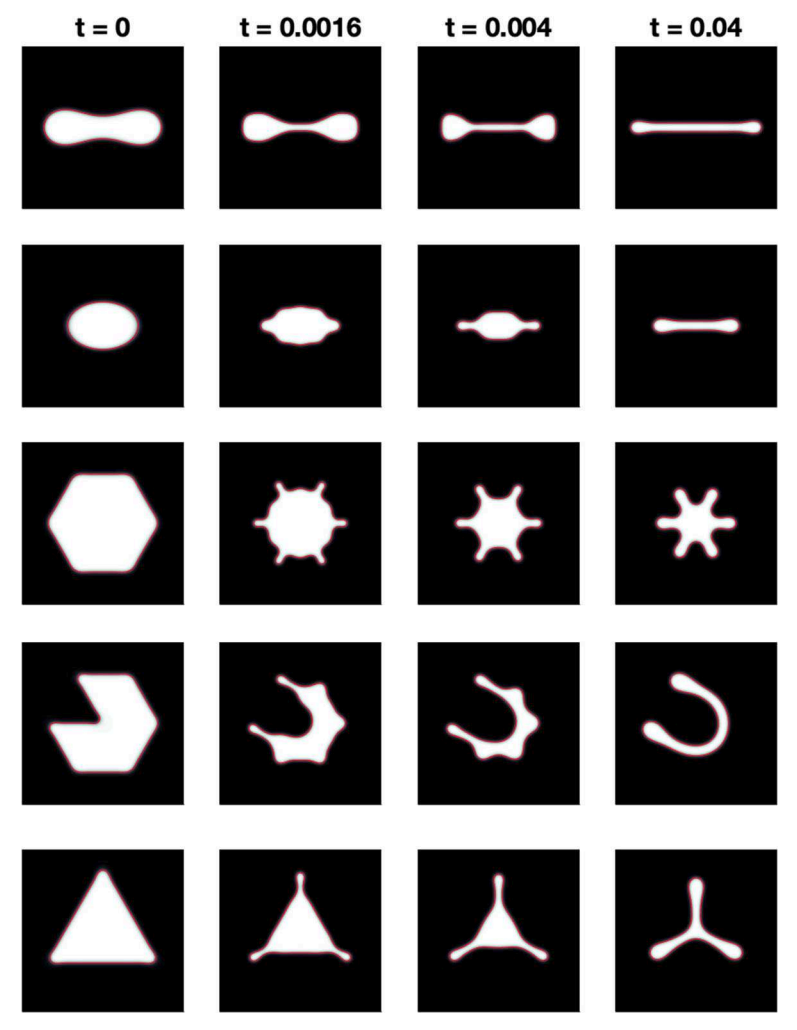


Fig. 12 Shape evolution of other shrink age examples with different initial morphology but same parameters as those used in Fig. 10. They have a similar pattern: the inner region shrinks for the decline of osmotic energy and the sharp corners shrink to form finger-like structure; the shrinking process is with preserved surface area and mass; the concentrations of the inner and outer phases evolve to the corresponding equilibrium values labelf

In Fig. 11e, we show that the concentrations inside and outside the interface approach the equilibrium values ψ_{\star}^{in} and $\psi_{\star}^{\text{out}}$, respectively.

In Fig. 12, we present shape evolution of several other shrinkage examples with different initial morphology. They all follow the similar pattern: the white region will shrink for the decline of osmotic energy; the sharp corners will shrink to form finger-like structures; the shrinking process is always associated with arclength constraint and total mass conservation. Note that the concentrations of the inner and outer phases evolve to their corresponding equilibrium values.



97 Page 28 of 31 X. Tang et al.

5 Conclusion

In this paper, we have developed a phase field model for vesicle growth or shrinkage based on osmotic pressure that arises due to a chemical potential gradient. The primary contribution is that we defined a novel form of osmotic energy (2.3) with two simple quadratic functions (2.4). This allows us to control precisely the conditions for vesicle volume growth or shrinkage, as determined by the common tangent construction. The model is comprised of an Allen–Cahn-type equation, coupled to a Cahn–Hilliard-type equation. We exhibited an implicit-explicit (IMEX) scheme and implemented a fast nonlinear FAS multigrid method to update the system at each time step. We showed detailed convergence tests for the solver and discretization scheme, and we presented simulations of the evolution of the vesicle under growth or shrinkage conditions. The proposed model provides an effective way for describing vesicle growth or shrinkage in different situations by changing the parameters in the free energy.

Our IMEX scheme is obtained by balancing practical considerations, but it lacks a theoretical analysis for stability. In the future, we plan to construct a new scheme based on a convex splitting method of the discrete energy, or via an SAV-type approach, so as to achieve theoretically provable energy stability. For the former, we will use the papers (Wise 2010; Hu et al. 2009) for guidance. The convex splitting procedure requires writing the energy as the difference of purely convex pieces. It is straightforward to split the energy F^{surf} (Wise 2010). There also exists a procedure for splitting F^{bend} (Feng et al. 2018). One key difficulty associated with the convex splitting of F^{bend} is that a nonlinear energy functional term in the expansion is neither convex nor concave. To overcome this subtle difficulty, two auxiliary terms were added to make the combined term convex in Feng et al. (2018), which in turns yields a convex-concave decomposition of the energy. In our model, it will be even more complex for the convex splitting due to the fact that several terms in the energies F^{area} , and F^{osm} are indefinite. We will construct the convex pieces by adding auxiliary terms as suggested in Feng et al. (2018). The SAV methodology of Shen and others offers a different strategy for energy stability; and the key feature of that approach is that the resulting equations are typically linear (Shen et al. 2018).

Second-order schemes will be used in the future, even if these are based on linear IMEX constructions that may not lead to theoretical energy stability. It may be possible to construct higher-order (in time) schemes with unique solvability and energy stability properties as suggested in Guo et al. (2016), Yan et al. (2018), Guo et al. (2021), Cheng et al. (2019), Shen et al. (2018). But these would be highly non-trivial. We plan to investigate these issues in the next paper. In addition, we plan to extend this work to 3D and a more complex temporal evolution by adding a Stokes-like equation, following some ideas used in Chen et al. (2015), Yang (2021). This fluid–structure interaction type model will enable a better realization of vesicle dynamics. The current model, which is based only on diffusion, captures the free energy dissipation and may only accurately predict equilibria. Furthermore, one could modify the model so that purely biological considerations could alter the parameters so as to effect growth or shrinkage based on a changing fluid microenvironment for the vesicle. This would require the coupling of more biophysical equations to determine, for example, the electrolyte concentrations dynamically.



Acknowledgements SL acknowledges the support from the National Science Foundation (NSF), Division of Mathematical Sciences Grant DMS-1720420. SL was also partially supported by Grant ECCS-1307625. SMW acknowledges support from NSF Grant, DMS 2012634. JL acknowledges partial support from the NSF through Grants DMS-1714973, DMS-1719960, and DMS-1763272 and the Simons Foundation (594598QN) for a NSF-Simons Center for Multiscale Cell Fate Research. JL also thanks the National Institutes of Health for partial support through grants 1U54CA217378-01A1 for a National Center in Cancer Systems Biology at UC Irvine and P30CA062203 for the Chao Family Comprehensive Cancer Center at UC Irvine.

Declarations

Conflict of interest The authors declare that we have no known conflicts of interest regarding the submission of this manuscript.

References

- Alberts B, Heald R, Johnson A, Morgan D, Raff M, Roberts K, Walter P (2022) Molecular biology of the cell, 7th edn. W. W. Norton and Company, New York
- Bartels S (2015) The Allen–Cahn equation. In: Numerical methods for nonlinear partial differential equations, vol 47. Springer, Cham, pp 153–182. https://doi.org/10.1007/978-3-319-13797-16
- Baumgarten CM, Feher JJ (2012) Chapter 16—Osmosis and regulation of cell volume. In: Sperelakis N (ed) Cell physiology source book, 4th ed. Academic Press, San Diego, pp 261–301. https://doi.org/10.1016/B978-0-12-387738-3.00016-0
- Cahn JW, Hilliard JE (1958) Free energy of a nonuniform system. I. Interfacial free energy. J Chem Phys 28:258–267. https://doi.org/10.1063/1.1744102
- Chen R, Ji G, Yang X, Zhang H (2015) Decoupled energy stable schemes for phase-field vesicle membrane model. J Comput Phys 302:509–523. https://doi.org/10.1016/j.jcp.2015.09.025
- Cheng K, Feng W, Wang C, Wise SM (2019) An energy stable fourth order finite difference scheme for the Cahn–Hilliard equation. J Comput Appl Math 362:574–595. https://doi.org/10.1016/j.cam.2018.05.039
- Du Q, Liu C, Wang X (2004) A phase field approach in the numerical study of the elastic bending energy for vesicle membranes. J Comput Phys 198:450–468. https://doi.org/10.1016/j.jcp.2004.01.029
- Du Q, Liu C, Ryham R, Wang X (2005) A phase field formulation of the Willmore problem. Nonlinearity 18:1249–1267. https://doi.org/10.1088/0951-7715/18/3/016
- Elani Y, Law RV, Ces O (2014) Vesicle-based artificial cells as chemical microreactors with spatially segregated reaction pathways. Nat Commun 5:5305. https://doi.org/10.1038/ncomms6305
- Feng W, Guan Z, Lowengrub J, Wang C, Wise S, Chen Y (2018) A uniquely solvable, energy stable numerical scheme for the functionalized Cahn–Hilliard equation and its convergence analysis. J Sci Comput 76:1938–1967. https://doi.org/10.1007/s10915-018-0690-1
- Gera P, Salac D (2018) Three-dimensional multicomponent vesicles: dynamics and influence of material properties. Soft Matter 14:7690–7705. https://doi.org/10.1039/C8SM01087K
- Gera P, Salac D, Spagnolie SE (2022) Swinging and tumbling of multicomponent vesicles in flow. J Fluid Mech 935:A39. https://doi.org/10.1017/jfm.2022.40
- Giga M-H, Kirshtein A, Liu C (2017) Variational modeling and complex fluids. In: Giga Y, Novotny A (eds) Handbook of mathematical analysis in mechanics of viscous fluids. Springer, Cham, p 141. https://doi.org/10.1007/978-3-319-10151-42-1
- Gu R, Wang X, Gunzburger MD (2016) A two phase field model for tracking vesicle-vesicle adhesion. J Math Biol 73:1293–1319. https://doi.org/10.1007/s00285-016-0994-4
- Guo J, Wang C, Wise SM, Yue X (2016) An H2 convergence of a second-order convex-splitting, finite difference scheme for the three-dimensional Cahn–Hilliard equation. Commun Math Sci 14:66. https://doi.org/10.4310/CMS.2016.v14.n2.a8
- Guo M et al (2017) Cell volume change through water efflux impacts cell stiffness and stem cell fate. PNAS 114:E8618–E8627. https://doi.org/10.1073/pnas.1705179114



97 Page 30 of 31 X. Tang et al.

Guo J, Wang C, Wise SM, Yue X (2021) An improved error analysis for a second-order numerical scheme for the Cahn–Hilliard equation. J Comput Appl Math 388:113–300. https://doi.org/10.1016/j.cam. 2020.113300

- Haußer F, Marth W, Li S, Lowengrub J, Rätz A, Voigt A (2013) Thermodynamically consistent models for two-component vesicles. Int J Biomath Biostat 2:1948
- Henson VE (2003) Multigrid methods nonlinear problems: an overview. In: Bouman CA, Stevenson RL (eds) Computational imaging, vol 5016. SPIE, p 3648. https://doi.org/10.1117/12.499473
- Hoffmann EK, Lambert IH, Pedersen SF (2009) Physiology of cell volume regulation in vertebrates. Physiol Rev 89:193–277. https://doi.org/10.1152/physrev.00037.2007
- Hu Z, Wise S, Wang C, Lowengrub J (2009) Stable and efficient finite-difference nonlinear-multigrid schemes for the phase-field crystal equation. J Comput Phys 228:5323–5339. https://doi.org/10.1016/ j.jcp.2009.04.020
- Jayathilake P G, Khoo B, Tan Z (2010a) Effect of membrane permeability on capsule substrate adhesion: computation using immersed interface method. Chem Eng Sci 65:3567–3578. https://doi.org/10.1016/j.ces.2010.02.050
- Jayathilake PG, Tan Z, Khoo B, Wijeysundera N (2010b) Deformation and osmotic swelling of an elastic membrane capsule in Stokes flows by the immersed interface method. Chem Eng Sci 65:1237–1252. https://doi.org/10.1016/j.ces.2009.09.078
- Kay D, Welford R (2006) A multigrid finite element solver for the Cahn–Hilliard equation. J Comput Phys 212:288–304. https://doi.org/10.1016/j.jcp.2005.07.004
- Kobayashi R (2010) A brief introduction to phase field method. AIP Conf Proc 1270:282–291. https://doi.org/10.1063/1.3476232
- LadyofHats (2007) Tonicity Wikipedia, The Free Encyclopedia. https://en.wikipedia.org/wiki/File: Osmoticpressureonbloodcellsdiagram.svg. Accessed 11 Sept 2020
- Layton AT (2006) Modeling water transport across elastic boundaries using an explicit jump method. SISC 28:2189–2207. https://doi.org/10.1137/050642198
- Lee D, Huh J-Y, Jeong D, Shin J, Yun A, Kim J (2014) Physical, mathematical, and numerical derivations of the Cahn–Hilliard equation. Comput Mater Sci 81:216–225. https://doi.org/10.1016/j.commatsci. 2013.08.027
- Li S, Lowengrub J, Voigt A (2012) Locomotion, wrinkling, and budding of a multicomponent vesicle in viscous fluids. Comm Math Sci 10:645–670. https://doi.org/10.4310/CMS.2012.v10.n2.a11
- Liu K, Li S (2014) Nonlinear simulations of vesicle wrinkling. Math Methods Appl Sci 37:1093–1112. https://doi.org/10.1002/mma.2867
- Liu K, Hamilton C, Allard J, Lowengrub J, Li S (2016) Wrinkling dynamics of fluctuating vesicles in time dependent viscous flow. Soft Matter 12:5663–5675. https://doi.org/10.1039/C6SM00499G
- Liu K, Marple GR, Allard J, Li S, Veerapaneni S, Lowengrub J (2017) Dynamics of a multicomponent vesicle in shear flow. Soft Matter 13:3521–3531. https://doi.org/10.1039/C6SM02452A
- Lowengrub J, Rätz A, Voigt A (2009) Phase-field modeling of the dynamics of multicomponent vesicles: spinodal decomposition, coarsening, budding, and fission. Phys Rev E Stat Nonlinear Soft Matter Phys 79: 031926. https://doi.org/10.1103/PhysRevE.79.031926
- Mori Y, Liu C, Eisenberg R (2011) A model of electrodiffusion and osmotic water flow and its energetic structure. Phys D Nonlinear Phenom 240:1835–1852. https://doi.org/10.1016/j.physd.2011.08.010
- Pelton AD (2019) Phase diagrams and thermodynamic modeling of solutions. Elsevier, Amsterdam. https://doi.org/10.1016/C2013-0-19504-9
- Peskin CS (1977) Numerical analysis of blood flow in the heart. J Comput Phys 25:220–252. https://doi.org/10.1016/0021-9991(77)90100-0
- Provatas N, Elder K (2010) Phase-field methods in materials science and engineering. Wiley, New York. https://doi.org/10.1002/9783527631520
- Quaife B, Gannon A, Young Y-N (2021) Hydrodynamics of a semipermeable inextensible membrane under flow and confinement. Phys Rev Fluids 6:073601. https://doi.org/10.1103/PhysRevFluids.6.073601
- Salac D, Miksis M (2011) A level set projection model of lipid vesicles in general flows. J Comput Phys 230:8192–8215. https://doi.org/10.1016/j.jcp.2011.07.019
- Shen J, Yang X, Wang Q (2012) Mass and volume conservation in phase field models for binary fluids. Commun Comput Phys 13:1045–1065. https://doi.org/10.4208/cicp.300711.160212a
- Shen J, Xu J, Yang J (2018) The scalar auxiliary variable (SAV) approach for gradient flows. J Comput Phys 353:407–416. https://doi.org/10.1016/j.jcp.2017.10.021



- Sohn JS, Tseng Y-H, Li S, Voigt A, Lowengrub JS (2010) Dynamics of multicomponent vesicles in a viscous fluid. J Comput Phys 229:119–144. https://doi.org/10.1016/j.jcp.2009.09.017
- Sohn J, Li S, Li X, Lowengrub J (2012) Dynamics of multicomponent vesicles in a viscous fluid. Int J Numer Methods Biomed Eng 28:346–368. https://doi.org/10.1002/cnm.2475
- Strange K (2004) Cellular volume homeostasis. Adv Physiol Educ 28:155–159. https://doi.org/10.1152/advan.00034.2004
- Trottenberg U, Oosterlee CW, Schüller A (2001) Multigrid. Academic Press, San Diego
- Veerapaneni SK, Gueyffier D, Biros G, Zorin D (2009) A numerical method for simulating the dynamics of 3D axisymmetric vesicles suspended in viscous flows. J Comput Phys 228:7233–7249. https://doi.org/10.1016/j.jcp.2009.06.020
- Veerapaneni SK, Gueyffier D, Zorin D, Biros G (2009) A boundary integral method for simulating the dynamics of inextensible vesicles suspended in a viscous fluid in 2D. J Comput Phys 228:2334–2353. https://doi.org/10.1016/j.jcp.2008.11.036
- Vogl CJ, Miksis MJ, Davis SH, Salac D (2014) The effect of glass-forming sugars on vesicle morphology and water distribution during drying. J R Soc Interface 11:66. https://doi.org/10.1098/rsif.2014.0646
- Wang X, Du Q (2008) Modelling and simulations of multi-component lipid membranes and open membranes via diffuse interface approaches. J Math Biol 56:34771. https://doi.org/10.1007/s00285-007-0118-2
- Wang X, Gong X, Sugiyama K, Takagi S, Huang H (2020) An immersed boundary method for mass transfer through porous biomembranes under large deformations. J Comput Phys 413:109–444. https://doi.org/10.1016/j.jcp.2020.109444
- Wise SM (2010) Unconditionally stable finite difference, nonlinear multigrid simulation of the Cahn–Hilliard–Hele–Shaw system of equations. J Sci Comput 44:3668. https://doi.org/10.1007/s10915-010-9363-4
- Yan Y, Chen W, Wang C, Wise SM (2018) A second-order energy stable BDF numerical scheme for the Cahn-Hilliard equation. Commun Comput Phys 23:572–602. https://doi.org/10.4208/cicp.OA-2016-0197
- Yang X (2021) Numerical approximations of the Navier–Stokes equation coupled with volume-conserved multi-phase-field vesicles system: fully-decoupled, linear, unconditionally energy stable and secondorder time-accurate numerical scheme. Comput Methods Appl Mech Eng 375:113600. https://doi. org/10.1016/j.cma.2020.113600
- Yao L, Mori Y (2017) A numerical method for osmotic water flow and solute diffusion with deformable membrane boundaries in two spatial dimension. J Comput Phys 350:728–746. https://doi.org/10.1016/j.jcp.2017.09.006

Publisher's Note Springer Nature remains neutral with regard to jurisdictional claims in published maps and institutional affiliations.

Springer Nature or its licensor (e.g. a society or other partner) holds exclusive rights to this article under a publishing agreement with the author(s) or other rightsholder(s); author self-archiving of the accepted manuscript version of this article is solely governed by the terms of such publishing agreement and applicable law.

